The Astrophysical Journal, 941:95 (27pp), 2022 December 10 https://doi.org/10.3847/1538-4357/ac9cd5

An Elusive Population of Massive Disk Galaxies Hosting Double-lobed Radio-loud Active Galactic Nuclei

Zihao Wu[1], Luis C. Ho[1,2], and Ming-Yang Zhuang[1,2]
[1] Department of Astronomy, School of Physics, Peking University, Beijing 100871, People's Republic of China; zhwu@pku.edu.cn
[2] Kavli Institute for Astronomy and Astrophysics, Peking University, Beijing 100871, People's Republic of China
Received 2022 September 5; revised 2022 October 20; accepted 2022 October 20; published 2022 December 30

Abstract

It is commonly accepted that radio-loud active galactic nuclei are hosted exclusively by giant elliptical galaxies. We analyze high-resolution optical Hubble Space Telescope images of a sample of radio galaxies with extended double-lobed structures associated with disk-like optical counterparts. After systematically evaluating the probability of chance alignment between the radio lobes and the optical counterparts, we obtain a sample of 18 objects likely to have genuine associations. The host galaxies have unambiguous late-type morphologies, including spiral arms, large-scale dust lanes among the edge-on systems, and exceptionally weak bulges, as judged by the low global concentrations, small global Sérsic indices, and low bulge-to-total light ratios (median $B/T = 0.13$). With a median Sérsic index of 1.4 and low effective surface brightnesses, the bulges are consistent with being pseudobulges. The majority of the hosts have unusually large stellar masses (median $M_* = 1.3 \times 10^{11}\, M_\odot$) and red optical colors (median $g - r = 0.69$ mag), consistent with massive, quiescent galaxies on the red sequence. We suggest that the black hole mass (stellar mass) plays a fundamental role in launching large-scale radio jets, and that the rarity of extended radio lobes in late-type galaxies is the consequence of the steep stellar mass function at the high-mass end. The disk radio galaxies have mostly Fanaroff–Riley type II morphologies yet lower radio power than sources of a similar type traditionally hosted by ellipticals. The radio jets show no preferential alignment with the minor axis of the galactic bulge or disk, apart from a possible mild tendency for alignment among the most disk-dominated systems.

Unified Astronomy Thesaurus concepts: Radio jets (1347); Radio loud quasars (1349); AGN host galaxies (2017); Active galactic nuclei (16); Galaxy nuclei (609); Radio active galactic nuclei (2134); Radio galaxies (1343); Galaxy masses (607); Active galaxies (17); Quasars (1319)

1. Introduction

Massive black holes (BHs) lurk at the center of all massive galaxies (Kormendy & Ho 2013) and even in a significant fraction of less massive systems (Greene et al. 2020). Mass accretion onto the BH generates nuclear activity that gives rise to a plethora of energetic phenomena associated with active galactic nuclei (AGNs). One of the most enduring unsolved problems is the origin of radio jets, a distinctive feature of some but not all AGNs (Urry & Padovani 1995). AGNs are conventionally designated as either radio-loud or radio-quiet, even if there is strong motivation to abandon these labels in favor of more physical alternatives (for a recent perspective, see Padovani 2017). For historical reasons, two operational definitions of radio-loudness have been commonly invoked. On the one hand, radio-loudness can be demarcated on the basis of an absolute radio power, such as $P_{6\,\mathrm{cm}} > 10^{25}\,\mathrm{W\,Hz^{-1}\,sr^{-1}}$ (Miller et al. 1990). This has the advantage of simplicity and independence from observations at other wavelengths. On the other hand, it has become popular to define radio-loudness not by an absolute but instead by the relative strength of the radio emission. For instance, Kellermann et al. (1989) proposed the widely embraced convention of $R \equiv L_\nu(6\,\mathrm{cm})/L_\nu(B)$, with the boundary between radio-loud versus radio-quiet set at $R = 10$. By this criterion, ∼10%–20% of optically selected quasars are radio-loud (e.g., Visnovsky et al. 1992; Hooper et al. 1995). Both of these traditional criteria encounter difficulties once we confront AGNs of lower luminosity drawn from BHs of lower mass or lower accretion rate. For the vast majority of the galaxy population and for most of their lifecycle, the radio-loudness of an AGN cannot be measured accurately without taking host galaxy contamination into account (e.g., Ho & Peng 2001). Notwithstanding these complications, a distinctive empirical trend regarding the nature of radio jets has remained largely intact: the most powerful radio-loud AGNs, especially those that sport large-scale, double-lobed hotspots that extend beyond the confines of the host galaxy, reside nearly universally in elliptical galaxies, while the host galaxies of the radio-quiet counterparts span a wide range of optical morphologies (e.g., McLure et al. 1999; Kim et al. 2017). The dichotomy in the host morphology in terms of radio-loudness has long been recognized in radio galaxies (Matthews et al. 1964; Zirbel 1996; McLure et al. 2004) and confirmed by high-resolution observations of the hosts of radio-loud quasars (McLure et al. 1999; Hamilton et al. 2002; Dunlop et al. 2003) and BL Lac objects (Urry et al. 2000). Throughout this paper, we restrict our attention to the class of radio-loud AGNs typified by extended, double-lobed radio jets.

What is the physical basis for this observational trend? The leading model suggests that powerful, relativistic jets in radio-loud AGNs form by tapping into the rotational energy of a rapidly spinning BH (Blandford & Znajek 1977). In an attempt to link radio-loudness with galaxy morphology, Wilson & Colbert (1995) proposed that radio-loud AGNs are uniquely associated with elliptical galaxies because their central BHs have been spun up by galaxy–galaxy major mergers. Spiral galaxies, on the other hand, cannot spin up BHs because they evolve largely through internal secular processes. Wilson & Colbert's merger-driven mechanism of generating BH spin explains why spiral galaxies cannot host radio-loud AGNs. Baum et al. (1995) further suggested that the spin paradigm may further be able to account for the difference in radio power between (Fanaroff & Riley 1974; FR) type I and type II radio galaxies: FR IIs are more powerful than FR Is because they have more rapidly spinning BHs.

Recent advances in BH spin measurements have severely challenged this spin paradigm. Although the number of supermassive BHs with reliable spin measurements is still quite limited, the extant evidence suggests that many supermassive BHs, at least in the nearby universe, are rapidly spinning objects (Reynolds 2019, 2021), with a significant fraction hosted by spiral galaxies (e.g., Marinucci et al. 2014; Walton et al. 2014; Vasudevan et al. 2016; Buisson et al. 2018; Jiang et al. 2019). Notably, recent observations from the Event Horizon Telescope (Akiyama et al. 2022) reveal that the central BH of our own Galaxy, Sgr A*, itself has a high spin. In light of these developments, it is no longer tenable to invoke the spin paradigm to account for the morphology dichotomy between radio-loud and radio-quiet AGNs.

Perhaps the BH mass, not spin, determines jet power. After all, the fraction of galaxies that hosts radio-loud AGNs depends strongly on the stellar mass (Scarpa & Urry 2001; Best et al. 2005; Mauch & Sadler 2007). Now, to the extent that the BH mass is closely linked with the stellar mass (Magorrian et al. 1998; Kormendy & Ho 2013), it is tempting to conclude that more massive BHs are more prone to producing radio-loud AGNs. Moreover, the very power of the radio jet increases with the BH mass (e.g., Franceschini et al. 1998; Lacy et al. 2001; McLure & Jarvis 2004). As late-type galaxies generally host less massive BHs (Greene et al. 2020), likely an indirect manifestation of their typically lower stellar masses (Moffett et al. 2016), it would be natural that disk-dominated galaxies can only sustain less powerful, and hence less extended (Ledlow et al. 2002), radio jets. These expectations are merely indicative, at best, for they are based on statistical correlations with substantial scatter. Given the significant dispersion in the relation between the BH mass and radio luminosity (e.g., Ho 2002; Woo & Urry 2002) and the similarly loose correlation between the BH mass and galaxy stellar mass for late-type galaxies (Greene et al. 2020), we should remain open to the possibility that some late-type galaxies might host radio-loud AGNs.

What concrete evidence exists, then, that disk galaxies host radio-loud AGNs? Much attention has been cast on the so-called radio-loud narrow-line Seyfert 1 galaxies (NLS1s). NLS1s designate AGNs with relatively low BH masses and high accretion rates (e.g., Boroson 2002), which normally tend to be radio-quiet (Ulvestad et al. 1995; Greene et al. 2006). Consistent with their low BH masses, the hosts of NLS1s are generally disk galaxies (e.g., Orban de Xivry et al. 2011; Kim et al. 2017). A minority of NLS1s, however, exhibit blazar-like characteristics at radio and even γ-ray energies (e.g., Abdo et al. 2009; Foschini et al. 2015), strongly suggesting that at least in this subpopulation late-type galaxies can launch relativistic jets. If true, this would represent a fundamental paradigm shift. However, despite numerous efforts to characterize the structure and morphology of the host galaxies of radio-loud NLS1s, disentangling the host from the glare of the bright nucleus remains challenging using ground-based images, even under conditions of exceptionally good seeing and pushing the observing bandpass to the near-infrared. While some examples of disk hosts have emerged (e.g., Kotilainen et al. 2016; Vietri et al. 2022), others are still open to interpretation (e.g., León-Tavares et al. 2014; Järvelä et al. 2018; Olguín-Iglesias et al. 2020), raising doubts as to whether they are bona fide late-type disk galaxies (Tadhunter 2016). The situation is considerably simpler in the case of radio galaxies, whose orientation in the plane of the sky shields the bright nucleus from the viewer. To date, only a handful of cases of extended radio lobes have been reported to be hosted by disk galaxies (Ledlow et al. 1998; Hota et al. 2011; Bagchi et al. 2014; Mao et al. 2015; Singh et al. 2015; Mulcahy et al. 2016; Vietri et al. 2022). However, most discoveries lack detailed chance alignment analysis to confirm the radio associations, and the number of objects is too marginal for meaningful statistical analysis.

In this study, we present a sample of radio-loud AGNs with classical double-lobed radio structures that we can associate with high confidence with host galaxies having clearly late-type, disk-dominated optical morphology. These objects originate from a parent sample of objects initially selected by the Gems of Galaxy Zoo (Zoo Gems; Keel et al. 2022) project, which obtained high-resolution Hubble Space Telescope (HST) optical images of a collection of sources previously identified through the Radio Galaxy Zoo program (Banfield et al. 2015) to be double radio lobes apparently associated with late-type galaxies. We systematically and quantitatively analyze the HST images and estimate the probability of chance alignment for each object. From the original sample of 32 sources presented by Keel et al. (2022), we arrive at a high-confidence sample of 18 sources that we deem to be truly associated with the optical counterpart imaged with HST. We demonstrate that extremely late-type disk galaxies can indeed produce extended radio jets, but these galaxies turn out to be very massive and mostly red. We argue that the BH mass, not only the BH spin, is a key factor governing jet production.

The paper is structured as follows. Section 2 summarizes the observations used in this paper. We evaluate the probability of chance alignment and establish a high-confidence sample in Section 3. We describe our measurements of the radio and optical images in Section 4 and present the statistical properties of the host galaxies and radio sources in Section 5. Section 6 discusses the connection between launching radio lobes and the physical properties of the host galaxies. This paper adopts a Chabrier (2003) stellar initial mass function and a ΛCDM cosmology with $H_0 = 69$ km s^{-1} Mpc^{-1}, $\Omega_{\rm m} = 0.29$, and $\Omega_\Lambda = 0.71$ based on the final nine-year Wilkinson Microwave Anisotropy Probe observations (Hinshaw et al. 2013).

2. Observations

Our sample is based on the Radio Galaxy Zoo and the Zoo Gems projects. Radio Galaxy Zoo is an online citizen-science program that invites volunteers to identify infrared and optical counterparts of radio sources in the Faint Images of the Radio Sky at Twenty Centimeters (FIRST; Becker et al. 1995) survey. The FIRST survey gives snapshots of the sky in the 1.4 GHz band with an exposure time of 3 minutes, which typically generates images with a FWHM beam size of 5$''$.4, an astrometric accuracy of 50 mas, and rms noise of

0.15 mJy beam^{-1}. Radio Galaxy Zoo includes all spatially resolved radio sources in the FIRST survey with signal-to-noise ratios higher than 10. The radio images are fed to volunteers to locate the host galaxies by overlaying them with optical images from data release 10 (Ahn et al. 2014) and data release 12 (Alam et al. 2015) of the Sloan Digital Sky Survey (SDSS) and with near-infrared images from the Wide-Field Infrared Survey Explorer (WISE; Wright et al. 2010).

Zoo Gems is a follow-up project of Radio Galaxy Zoo that makes use of short windows in the HST schedule to observe galaxies with peculiar morphologies of interest. Before the start of Zoo Gems, roughly half of the candidate FIRST sources had host identifications and were sent to the data pool of Zoo Gems for further analysis. Zoo Gems selected 32 double-lobed radio sources apparently associated with a host galaxy having a prominent disk component, according to analysis based on the SDSS pipeline and two-dimensional fits using GALFIT (Peng et al. 2002, 2010). HST observations of 674 s duration were obtained in the F475W filter (close to the SDSS g band) using the Wide-Field Camera mode of the Advanced Camera for Surveys (Ford et al. 1998). A two-point dither pattern was adopted to better sample the point-spread function. The images have a pixel scale of 0.″05, a resolution of FWHM $\approx$ 0.″10–0.″14, and an astrometry accuracy of $\lesssim$10 mas. Using these 32 objects as our initial sample, we retrieved the radio images from the FIRST archive[3] and the optical HST images from the Mikulski Archive for Space Telescopes (MAST).[4] Figure 1 displays the HST images overlaid with the FIRST radio contours, for the subset of 18 sources we regard as having genuine optical–radio association (see details in Section 3); the images for the objects with less confident association are presented in Appendix A.

All galaxies have SDSS multiband photometry, and for our purposes we collect their `model` magnitudes in the g, r, and i bands (Table 1). Only 11 objects have spectroscopic redshifts ($z_{\rm spec}$). For the remaining 21 objects, we adopt photometric redshifts ($z_{\rm phot}$) from Duncan (2022), which is based on the Dark Energy Spectroscopic Instrument (DESI) Legacy Imaging Surveys (Dey et al. 2019). DESI covers most of the footprint of SDSS in grz, with 5σ point-source depths reaching $m_g = 24.7$, $m_r = 23.9$, $m_z = 23.0$ mag at 1.″5 seeing, ∼1.5 mag deeper than SDSS. Duncan (2022) derived photometric redshifts using a machine-learning technique, which is based on galaxy properties in the optical and mid-infrared bands, including color, magnitude, and size. Their photometric redshifts have a robust scatter compared with the spectroscopic redshift, with a normalized median absolute deviation $1.48 \times \text{median}(|z_{\rm phot} - z_{\rm spec}|/(1 + z_{\rm spec})) = 0.05$. Comparing $z_{\rm phot}$ with $z_{\rm spec}$ for the 11 objects with spectra yields good consistency with a scatter of only 0.01 for $(1+z)$.

For completeness, we note that there is a mismatch between the target names and sky coordinates in Table 2 of Keel et al. (2022). The names always lead to correct targets, as judged by the ancillary information available in the NASA/IPAC Extragalactic Database (NED). Some sources are named by radio programs (e.g., B3 0911+418), and their NED coordinates pertain to the center position of the radio emission instead of the optical center of the host galaxy. For consistency, all the updated coordinates in Table 1 refer to the position of the optical center of the galaxy.

[3] http://sundog.stsci.edu/cgi-bin/searchfirst

[4] https://mast.stsci.edu/search/hst/ui/

3. Sample Definition

The original sample of double-lobed radio sources from the Zoo Gems project was defined by their apparent association with an optically visible disk galaxy. To be fully convinced that the radio–optical association is real, we assess the probability that the galaxies we observe are aligned fortuitously with the radio lobes. The identification of the hosts of radio sources is usually based on the relative position between the radio emission and optically visible galaxies. However, because radio lobes lack emission lines to determine their redshift, the line-of-sight distance between the radio lobes and galaxies is unknown. Other sources along the line of sight might happen to be projected toward the radio center and be mistaken for the host galaxy. To statistically rule out such coincidences, we calculate the probability that the observed optical counterparts are chance-aligned, while the true host galaxies (assumed to be elliptical galaxies) are too faint to be detected. We use this chance alignment probability to define the final sample of galaxies included in this paper.

3.1. Probability of Disk Galaxies in Chance Alignment

We calculate the probability that an unrelated disk galaxy happens to be projected toward the center of the radio lobes. To begin with, the chance alignment probability depends on the number density of such galaxies. We use the Schechter (1976) luminosity function to calculate the number density of disk galaxies, which, in terms of magnitude, is (Loveday et al. 2012)

$$\phi(M) = 0.4 \ln 10 \; \phi^* \{10^{0.4(M^* - M)}\}^{\alpha+1} \exp\{-10^{0.4(M^* - M)}\}, \tag{1}$$

where M^* is the characteristic absolute magnitude, α is the power index, and ϕ^* is the normalization of the number density in units of Mpc^{-3}. We adopt the g-band luminosity function of blue galaxies from Loveday et al. (2012), for which $M^* - 5 \log h = -19.6$, $\phi^* = 7.1 \times 10^{-3}\, h^{-3}\,{\rm Mpc}^{-3}$, and $\alpha = -1.42$, with h the dimensionless Hubble constant. For galaxies brighter than a given apparent magnitude m_0, we calculate the surface number density $n(m \leqslant m_0)$ by integrating over all redshift range in a unit solid angle, taking the K-correction with a color $g - r = 0.66$ mag into account, typical of Sab galaxies (Fukugita et al. 1995).

Some galaxies have a radio core in their nucleus, but their number density is even smaller if their radio-loudness is high. Studying the radio-to-optical flux ratio

$$R_B = f_{1.4}/(k \cdot 10^{-0.4 m_B}), \tag{2}$$

where $f_{1.4}$ is the 1.4 GHz flux density in units of mJy, m_B is the B-band magnitude of the galaxy, and $k = 4.44 \times 10^6$ is a normalization factor, Gavazzi & Boselli (1999) found that only ∼0.4% of late-type galaxies have $R_B \geqslant 10$ and ∼4% have $R_B \approx$ 1–10. We derive the galaxy B-band magnitude from SDSS g and r magnitudes following Jester et al. (2005), after considering the K-correction and Galactic extinction. We measure the nuclear radio emission with the Common Astronomy Software Application (CASA; McMullin et al. 2007) and apply the K-correction assuming a spectral index of −0.8 (Blundell et al. 1999) to derive the radio luminosity. Note that here we assume that the associations with the radio lobes are unknown and only take the core radio emission into

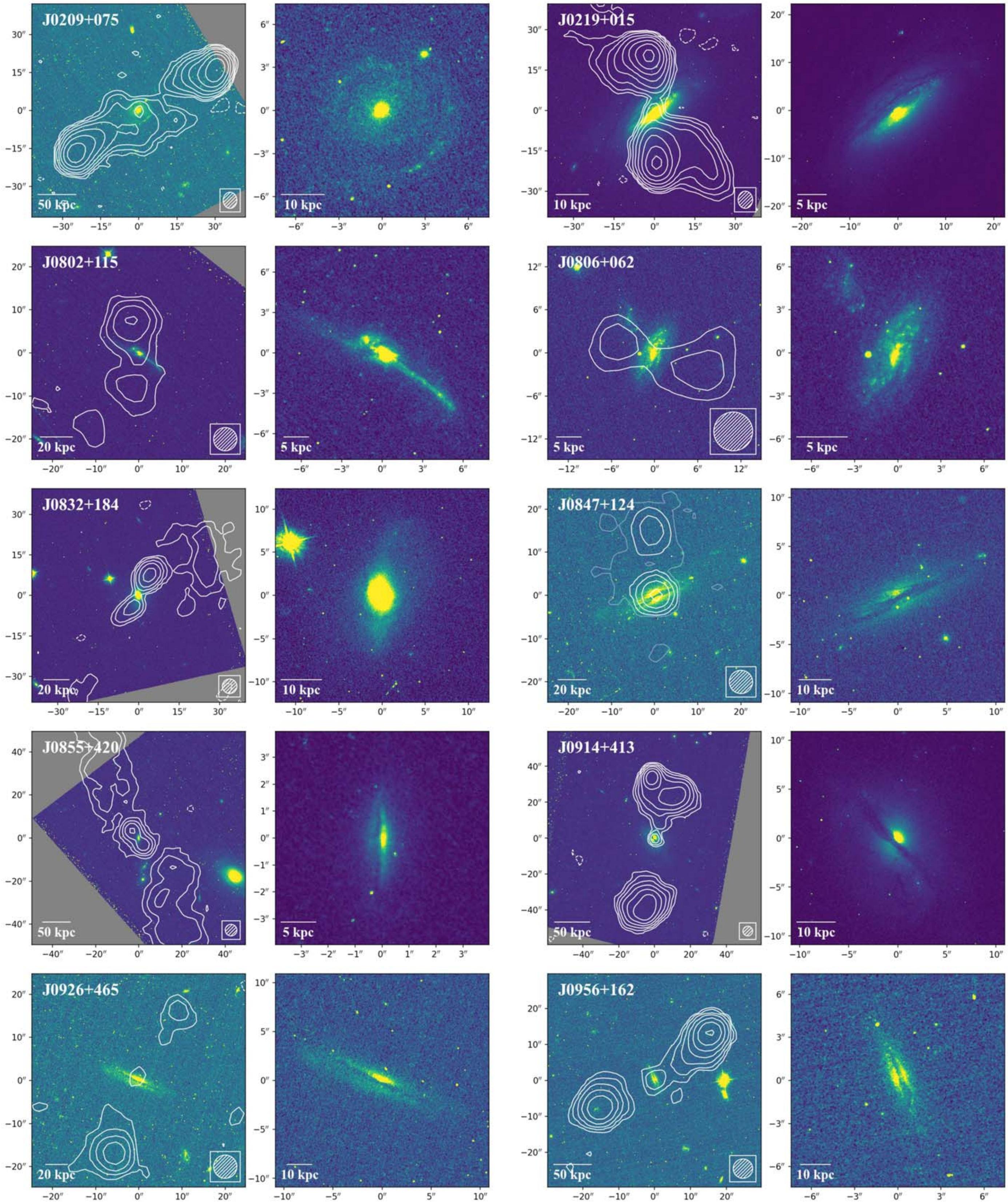

Figure 1. HST F475W images of the 18 high-confidence sources in our sample, overlaid with FIRST 1.4 GHz contours in the left panel and zoomed-in to highlight the optical morphology of the galaxy in the right panel. All images are centered on the galaxy with north up and east to the left. The restoring beam of the radio map is depicted as a hatched ellipse on the lower-right corner. The radio contours are (−3, 3, 6, 12, 24, 48, 96, ...) × rms of each image, where the values of the rms are listed in Table 3. Object J0847+124 shows an additional 1.5 rms contour in light-gray color. The scale bar in the lower-left corner of each panel indicates the proper distance at the redshift of each object. Figure A1 displays the low-confidence objects.

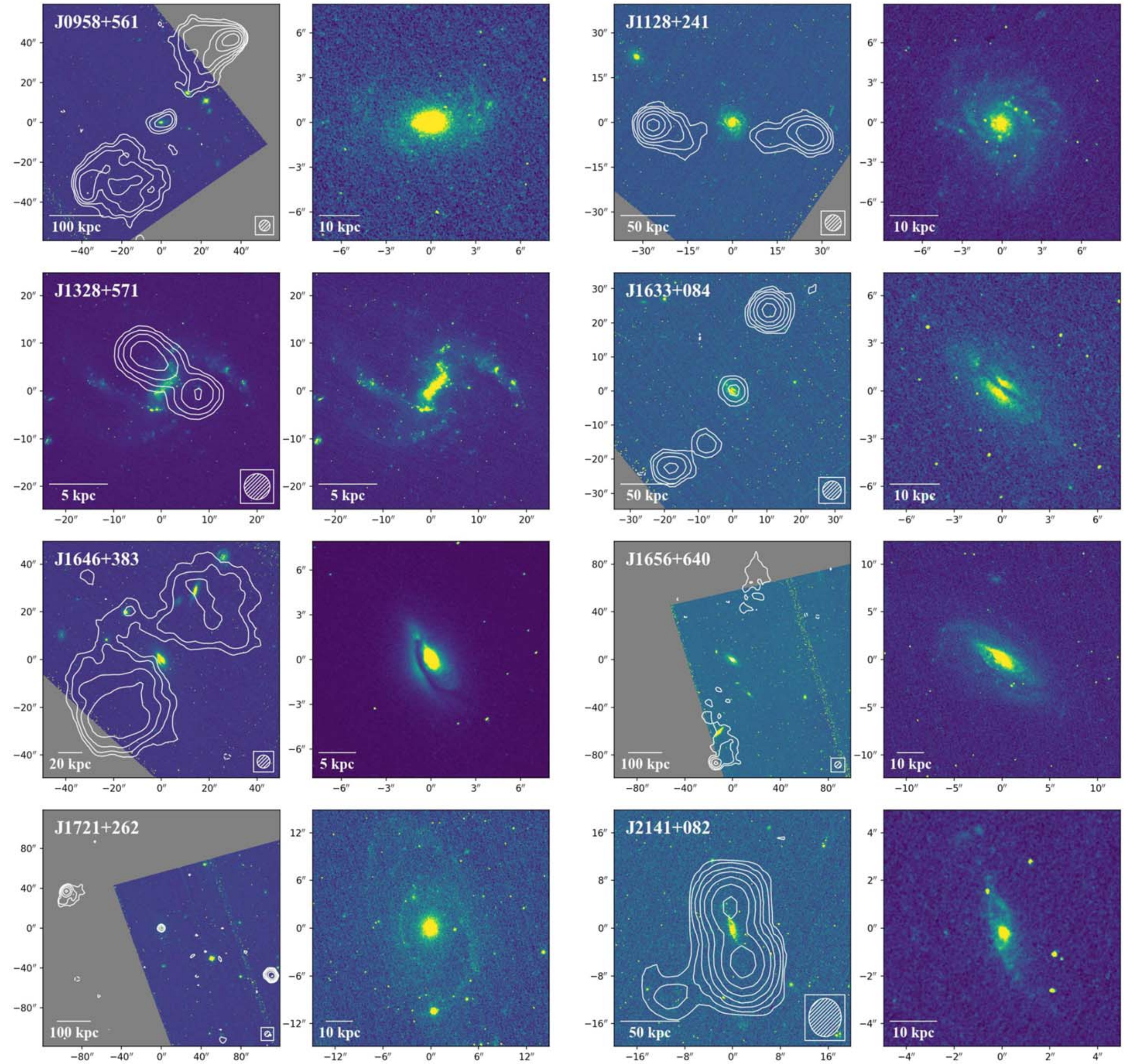

Figure 1. (Continued.)

consideration. Depending on the radio-loudness, we multiply the rarity factors (0.004 for $R_B \geqslant 10$ and 0.04 for $R_B = 1$–10) to their number density.

Finally, following Bloom et al. (2002) and Berger (2010), we calculate the probability that a galaxy coincides with the radio center within a separation r_{offset}:

$$p = 1 - e^{-\pi r_{\text{offset}}^2 n(m \leqslant m_{\text{gal}})} \approx \pi r_{\text{offset}}^2 n(m \leqslant m_{\text{gal}}), \tag{3}$$

where $n(m \leqslant m_{\text{gal}})$ in units of arcsec^{-2} is the surface number density of disk galaxies of the same or brighter magnitude, and r_{offset} is in units of arcsec. As in Laing et al. (1983), the radio center is defined as the midpoint of the two radio hotspots.

3.2. Probability of Observing No Elliptical Hosts

If the disk galaxies we observe are not the hosts of the radio lobes, the real hosts, which are usually giant elliptical galaxies, should appear in the deep HST images, unless they are too faint. Therefore, we estimate the probability distribution of the magnitude of possible elliptical hosts.

3.2.1. Probability Distribution of the Host Magnitude

The probability distribution of the luminosity for a galaxy is proportional to its luminosity function. Scarpa & Urry (2001) found that the luminosity function of radio elliptical galaxies correlates with that of normal elliptical galaxies as $A\phi(L)L^2$,

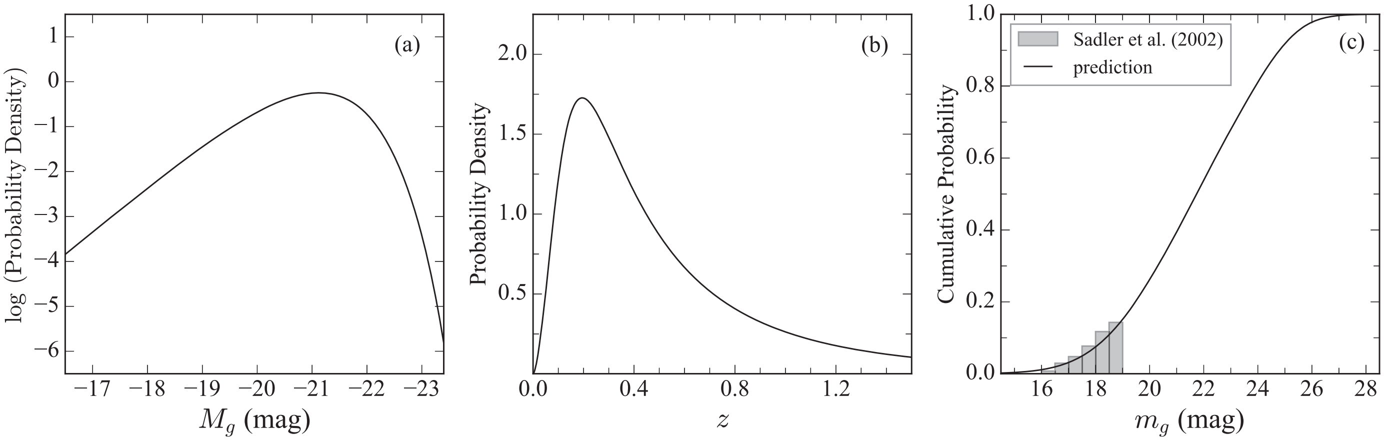

Figure 2. (a) Probability density as a function of the g-band absolute magnitude for red galaxies from Loveday et al. (2012). (b) Predicted probability density as a function of the redshift for galaxies with radio lobes and $S_{\rm tot} = 50$ mJy. (c) Cumulative probability distribution of a potential elliptical host of radio lobes as a function of the g-band apparent magnitude. Histograms denote objects with detected radio lobes and $S_{\rm tot} = 30$–70 mJy (Sadler et al. 2002).

Table 1
Basic Properties of the Sample

Name (1)	Full Name (2)	R. A. (J2000) ($^{\rm h\ m\ s}$) (3)	Decl. (J2000) ($^{\circ}\ '\ ''$) (4)	$z_{\rm phot}$ (5)	$z_{\rm spec}$ (6)	A_V (mag) (7)	m_g (mag) (8)	m_r (mag) (9)	m_i (mag) (10)
J0209+075	SDSS J020904.75+075004.5	02 09 04.75	07 50 04.5	0.251 ± 0.024	⋯	0.15	18.80	17.47	16.97
J0219+015	UGC 1797	02 19 58.73	01 55 48.7	0.033 ± 0.016	0.041	0.13	14.48	13.59	13.12
J0802+115	SDSS J080259.73+115709.7	08 02 59.73	11 57 09.7	0.173 ± 0.023	⋯	0.07	18.79	17.92	17.42
J0806+062	SDSS J080658.46+062453.4	08 06 58.46	06 24 53.4	0.112 ± 0.055	⋯	0.06	18.60	18.20	17.89
J0813+552	SDSS J081303.10+552050.7	08 13 03.10	55 20 50.7	0.279 ± 0.035	⋯	0.12	20.39	19.51	19.13
J0823+033	SDSS J082312.91+033301.3	08 23 12.91	03 33 01.3	0.122 ± 0.011	⋯	0.08	16.63	15.59	15.11
J0832+184	SDSS J083224.82+184855.4	08 32 24.82	18 48 55.4	0.122 ± 0.005	0.114	0.09	17.11	16.05	15.60
J0833+045	SDSS J083351.28+045745.4	08 33 51.28	04 57 45.4	0.246 ± 0.03	⋯	0.09	19.77	18.99	18.64
J0847+124	SDSS J084759.90+124159.3	08 47 59.90	12 41 59.3	0.157 ± 0.025	0.175	0.07	18.38	17.15	16.61
J0855+420	B3 0852+422	08 55 49.15	42 04 20.1	0.191 ± 0.025	⋯	0.08	19.45	18.14	17.55
J0901+164	SDSS J090147.17+164851.3	09 01 47.17	16 48 51.3	0.232 ± 0.026	⋯	0.08	19.28	18.26	17.79
J0903+432	SDSS J090305.84+432820.4	09 03 05.84	43 28 20.4	0.369 ± 0.041	0.373	0.05	20.70	19.17	18.46
J0914+413	B3 0911+418	09 14 45.54	41 37 14.3	0.149 ± 0.010	0.140	0.05	16.35	15.22	14.72
J0919+135	SDSS J091949.07+135910.7	09 19 49.07	13 59 10.7	0.417 ± 0.049	⋯	0.10	21.47	20.50	20.23
J0926+465	SDSS J092605.17+465233.9	09 26 05.17	46 52 33.9	0.202 ± 0.040	⋯	0.04	19.46	18.21	17.74
J0941+312	B2 0938+31A	09 41 03.63	31 26 18.7	0.366 ± 0.037	⋯	0.05	20.93	19.56	19.00
J0956+162	SDSS J095605.87+162829.9	09 56 05.87	16 28 29.9	0.341 ± 0.066	⋯	0.09	20.43	19.18	18.77
J0958+561	SDSS J095833.44+561937.8	09 58 33.44	56 19 37.8	0.247 ± 0.021	⋯	0.03	19.05	17.78	17.35
J1128+241	SDSS J112811.63+241746.9	11 28 11.63	24 17 46.9	0.121 ± 0.022	⋯	0.05	17.88	17.34	17.04
J1136+125	SDSS J113648.57+125239.7	11 36 48.57	12 52 39.7	0.059 ± 0.021	0.034	0.07	17.37	17.02	16.80
J1303+511	SDSS J130300.80+511954.7	13 03 00.80	51 19 54.7	0.122 ± 0.037	⋯	0.03	19.09	18.35	17.95
J1322+270	IC 4234	13 22 59.87	27 06 59.1	0.027 ± 0.005	0.034	0.06	14.26	13.63	13.31
J1328+571	SDSS J132809.31+571023.3	13 28 09.31	57 10 23.3	0.032 ± 0.029	⋯	0.03	16.91	16.78	16.69
J1349+454	SDSS J134900.13+454256.5	13 49 00.13	45 42 56.5	0.273 ± 0.042	⋯	0.04	20.83	19.45	18.85
J1354+465	B3 1352+471	13 54 36.02	46 57 01.5	0.180 ± 0.034	⋯	0.05	20.65	19.97	19.62
J1509+515	SDSS J150903.21+515247.9	15 09 03.21	51 52 47.9	0.575 ± 0.031	0.579	0.06	20.81	19.54	18.72
J1633+084	SDSS J163300.85+084736.4	16 33 00.85	08 47 36.4	0.266 ± 0.032	⋯	0.17	18.96	17.69	17.20
J1636+243	SDSS J163624.97+243230.8	16 36 24.97	24 32 30.8	0.118 ± 0.040	⋯	0.11	20.10	19.60	19.33
J1646+383	B2 1644+38	16 46 28.42	38 31 16.0	0.098 ± 0.021	0.108	0.04	17.51	16.63	16.17
J1656+640	SDSS J165620.60+640752.9	16 56 20.60	64 07 52.9	0.201 ± 0.018	0.212	0.07	17.98	16.90	16.40
J1721+262	SDSS J172107.89+262432.1	17 21 07.89	26 24 32.1	0.147 ± 0.011	0.170	0.11	18.78	17.68	17.18
J2141+082	SDSS J214110.61+082132.6	21 41 10.61	08 21 32.6	0.307 ± 0.043	⋯	0.15	20.22	19.11	18.43

Note. Col. (1): Abbreviated object name. Col. (2): Full object name from Keel et al. (2022). Cols. (3)–(4): Coordinates. Col. (5): Photometric redshift from the DESI survey. Col. (6): Spectroscopic redshift; all except object J0219+015 (Huchra et al. 1999) derive from SDSS. Col. (7): Galactic extinction from Schlafly & Finkbeiner (2011). Cols. (8)–(10): SDSS *gri*-band `model` magnitude after correction for Galactic extinction using the extinction curve of Cardelli et al. (1989).

with L the galaxy luminosity, $\phi(L)$ the luminosity function for normal elliptical galaxies, and a normalization factor A. We adopt $\phi(L)$ of red galaxies from Loveday et al. (2012) and derive the probability density distribution of absolute magnitude for radio elliptical galaxies (Figure 2(a)). Our order-of-magnitude estimates, which suffice for our purposes, do not consider the evolutionary effects of the luminosity function. Section 3.3 will show that this assumption provides a conservative estimate of chance alignment probability.

Meanwhile, we estimate the probability distribution of redshift based on the radio luminosity function and the observed radio flux density (Section 4). We describe the radio luminosity function as a double power law,

$$\Phi(L_{1.4}) = \frac{\Phi^*}{(L_{1.4}/L^*)^{\alpha} + (L_{1.4}/L^*)^{\beta}}, \tag{4}$$

where $L_{1.4}$ is the 1.4 GHz luminosity in units of W Hz^{-1}, L^* is the characteristic radio luminosity, and Φ^* is the characteristic number density. Following Mauch & Sadler (2007), we adopt $\Phi^* = 10^{-5.5}$ mag^{-1} Mpc^{-3}, $L^* = 10^{24.6}$ W Hz^{-1}, $\alpha = 1.27$, and $\beta = 0.49$. The probability that a radio source with a flux density S is at redshift z is proportional to the number of sources at that redshift:

$$p(z, S)dz\, dS = \frac{1}{\kappa}\,\Phi(L_{1.4})d\log L_{1.4}\, dV, \tag{5}$$

where κ is a normalization factor, $L_{1.4}$ and V are the corresponding absolute luminosity and comoving volume at redshift z, and $L_{1.4} = S\cdot 4\pi d_L/(1+z)^{1+\alpha}$, with d_L the luminosity distance and $\alpha = -0.8$ the spectral index (Blundell et al. 1999). Figure 2(b) shows the probability density as a function of the redshift, for a typical radio flux density in our sample, $S_{\rm tot} = 50$ mJy (Table 3). The probability peaks at $z \approx 0.2$ and decreases rapidly toward both lower and higher redshift.

Finally, we calculate the probability distribution of the apparent magnitude m by combining those of the absolute magnitude and the redshift, considering

$$m = M + \mu(z) + K(z), \tag{6}$$

where $\mu(z)$ is the distance modulus as a function of the redshift, defined as $\mu = 5\log(d_L/10\ {\rm pc})$, and $K(z)$ is the K-correction for elliptical galaxies, for which we use the spectral energy distribution (SED) templates generated using a delayed star formation history with an e-folding time of 2.5 Gyr. This set of templates is based on optical and near-infrared SEDs of elliptical and S0 galaxies in the Carnegie-Irvine Galaxy Survey (CGS; Ho et al. 2011), which match well the typical star formation history of early-type galaxies from the Galaxy And Mass Assembly survey (Bellstedt et al. 2020). We compare our probability distribution (Figure 2(c)) with a large sample of galaxies from the complete radio survey[5] of Sadler et al. (2002). We find excellent agreement between the observations and our model if we constrain the radio flux density to the same range ($S_{\rm tot} = 30$–70 mJy). Moreover, we note that the probability distribution is insensitive to the value of the observed radio flux density in the range of this sample (6–374 mJy). For instance, if $m_g < 25$ mag, the typical flux density (50 mJy) gives a probability $\sim$0.1, while the faintest case (6 mJy) gives a probability of $\sim$0.15. As we only need an order-of-magnitude estimate of the probability, we adopt the typical results for all objects.

[5] We transform their magnitudes in the b_J band to the g band assuming $b_J - g = 0.5$ mag (Jester et al. 2005; Chang et al. 2006).

3.2.2. Source Detection and Constraint on the Host Magnitude

Might the hosts of the radio sources actually be elliptical galaxies that have simply escaped detection? We use the `Python` source detection package `Photutils` (Bradley et al. 2020) to search a region centered at the midpoint of the radio hotspots. Defining d as the angular distance between the two hotspots, Laing et al. (1983) find that 96% of optical counterparts are distributed within 0.2 d from the radio center. We thus restrict our search to a radius of 0.2 d. We detect sources with a threshold set to 3 times the rms noise per pixel, requiring that the source contains 40 connected (0.1 arcsec^2) pixels, which is one-tenth of the minimal area of a galaxy of radius 5 kpc across the entire redshift range (the angular diameter scale peaks at 8.6 kpc arcsec^{-1} in our cosmology). We further crossmatch the detected sources with the DESI Legacy Imaging Surveys data release 8 (Duncan 2022) to obtain their redshift and exclude local small galaxies from candidate giant ellipticals, according to their absolute magnitude and size. Appendix B describes four positive detections of possible candidates. To be conservative, we view them as candidate hosts. For the other cases, we constrain the hypothetical elliptical galaxy host to be fainter than our detection limit, and we estimate the probability of it being so faint.

To estimate the detection limits, we randomly add simulated elliptical galaxies to the HST images and perform source detection as described above to determine the detection rate, which is defined as the percentage of detected cases. We use `GALFIT` to simulate single-component Sérsic (1968) models with index $n = 4$, as typically seen in elliptical galaxies (de Vaucouleurs 1948). We set the effective radii to $r_e = 3\farcs0$, $1\farcs6$, and $1\farcs2$, which correspond to typical radio galaxies with $r_e \approx 10$ kpc (McLure et al. 1999) at $z = 0.2$, 0.5, and 1.2. To examine our capability to detect sources with $m_g = 27$ mag, we simulate 100 mock elliptical galaxies for each r_e. All the HST images have detection rates higher than 97% for each value of r_e, which suggests that the detection limit is $\gtrsim$27 mag. Nevertheless, we do not adopt $m_g = 27$ mag as the detection limit in our analysis, as too many random sources (>1) would fall into our detection regions with this magnitude limit. Instead, we only regard sources brighter than 25 mag as candidate hosts. This much more conservative limit suffices for our chance alignment probability analysis and minimizes the number of confusing objects ($\lesssim$0.3) in our detection regions. We additionally consider the fact that our detection would be less sensitive if the sources overlap with a foreground disk galaxy, the likelihood of which depends on the size of the disk galaxy and the spatial distribution of the latent hosts. While 96% of optical counterparts are distributed within 0.2 d from the radio center (Laing et al. 1983), the chance of overlap is $\sim$50% when a disk galaxy with $r_e = 0.1\,d$ is located in the center. Therefore, the chance of overlap is significant for disk galaxies with $r_e > 0.1\,d$.

In the case of blended sources, we estimate the detection limit by adding simulated elliptical galaxies of increasing brightness to the region within the source's effective radius, until reaching the critical magnitude beyond which they are hardly discernible through visual inspection of the residual images from `GALFIT` decomposition (Section 4.2). Our tests indicate a limiting magnitude of $m_g \approx 22$. The probability of an elliptical host being fainter than the limit is 0.4, according to Figure 2(c). Incidentally, the specific value of the detection

Table 2
Sample Definition Based on Probability of Chance Alignment

Name (1)	$r_{\rm offset}$ ($''$) (2)	R_B (3)	Surface Density (deg^{-2}) (4)	Overlap (5)	P (6)	N_c (7)
High-confidence Sample						
J0847+124	0.7	23.8	24	H	4.6×10^{-9}	0.0002
J0219+015	1.1	···	0.17	H	2.0×10^{-8}	0.0010
J0914+413	5.4	3.9	2.06	L	5.8×10^{-8}	0.0029
J1633+084	3.7	21.5	49	L	6.6×10^{-8}	0.0033
J1646+383	0.9	···	8.1	L	1.6×10^{-7}	0.0080
J0956+162	2.7	56.1	248	L	1.7×10^{-7}	0.0087
J0958+561	7.5	43.9	56	L	3.0×10^{-7}	0.015
J1721+262	9.3	18.2	39	L	3.3×10^{-7}	0.016
J0832+184	1.4	···	5.0	H	9.4×10^{-7}	0.047
J0926+465	1.7	5.1	89	H	1.0×10^{-6}	0.050
J1656+640	9.5	$\lesssim$2	15	L	1.3×10^{-6}	0.065
J0806+062	0.7	···	31	H	1.5×10^{-6}	0.073
J0855+420	0.5	···	79	H	1.9×10^{-6}	0.096
J1128+241	2.6	···	13	L	2.2×10^{-6}	0.11
J2141+082	1.1	···	198	L	5.8×10^{-6}	0.29
J1328+571	4.0	···	3.9	H	6.0×10^{-6}	0.30
J0209+075	2.7	···	39	L	6.9×10^{-6}	0.34
J0802+115	1.5	···	39	H	8.5×10^{-6}	0.42
Low-confidence Sample						
J0833+045	2.4	···	126	L	1.8×10^{-5}	0.88
J1354+465	2.3	···	345	L	4.4×10^{-5}	2.2
J1636+243	3.8	···	177	L	6.2×10^{-5}	3.1
J0901+164	2.0	···	70	L	6.8×10^{-5}	3.4
J1136+125	7.2	···	7.2	L	9.0×10^{-5}	4.5
J1509+515	3.8	···	384	L	1.3×10^{-4}	6.7
J0813+552	1.6	···	248	L	1.5×10^{-4}	7.7
J0903+432	4.4	···	345	L	1.6×10^{-4}	8.1
J0919+135	18.1	$\lesssim$32	804	L	2.6×10^{-4}	13
J0941+312	8.2	···	428	L	7.0×10^{-4}	35
J0823+033	···	···	···	···	···	···
J1322+270	···	···	···	···	···	···
J1303+511	···	···	···	···	···	···
J1349+454	···	···	···	···	···	···

Note. Col. (1): Object name. Col. (2): Offset between the galaxy center and the midpoint of the radio lobes. Col. (3): Radio-loudness of the radio emission in the nuclear region, defined by Equation (2). Here we assume that the association with the radio lobes is unknown. Col. (4): Surface number density of galaxies of the same or brighter magnitude. Col. (5): Overlapping chance that a latent elliptical host galaxy hides behind the foreground galaxy: "L" = low chance of overlap, corresponding to a 0.1 probability of nondetection; "H" = high chance of overlap, corresponding to a 0.4 probability of nondetection. Col. (6): Chance alignment probability for a single case provided the radio–optical relative location and luminosity. Col. (7): Expected number of chance-aligned cases if selecting with criteria as in this case in the entire FIRST survey, which has $N \approx 5 \times 10^4$ pairs of double-lobed sources (McMahon et al. 2002); $N_c = P \times N$.

limit does not impact substantially our probability analysis for limiting magnitudes in the range $m_g \approx 20$–24 (Figure 2(c)). Although our estimate of the detection limit is approximate, it is sufficient for our analysis. In the end, we conclude that the nondetection probability is ∼0.4 when the chances of overlapping are high, and ∼0.1 when the chances are low.

3.3. Total Probability of Chance Alignment

We calculate the total probability of chance alignment P by multiplying the probability that a disk galaxy coincides with the radio center (Section 3.1) with the probability that an elliptical host galaxy is potentially present but too faint to be detected (Section 3.2). McMahon et al. (2002) detected a total of $N \approx 5 \times 10^4$ double-lobed sources in the FIRST survey. The expected number of chance-aligned events with properties specified for each object is therefore $N_c = P \times N$ (Table 2). We compile objects with $N_c < 0.5$ into the high-confidence sample and restrict our present analysis only to these. Assuming a Poisson distribution, the high-confidence sample has 90% probability of including no more than one dubious case. We note that there may be a few cases having real radio associations even in the low-confidence sample, as we have not taken other evidence, such as AGN activity and jet orientation, into consideration.

We conclude this section with a discussion of the evolutionary effects of the luminosity function on our probability estimation. Our results, which are based on a nonevolving luminosity function, are roughly consistent with those in an evolutionary framework because the radio sources are most likely located at low redshifts (Figure 2(b)). For a more quantitative estimation, we consider the evolving radio and optical luminosity functions of Ceraj et al. (2018) and Loveday et al. (2012), respectively. We find that the chance alignment probabilities decrease by ∼70%, which suggests that our previous estimation is very conservative. However, as the

Table 3
Measurement of Radio Properties

Name (1)	Beam ($'' \times ''$) (2)	rms (mJy beam^{-1}) (3)	FR Type (4)	d ($''$) (5)	D (kpc) (6)	PA (°) (7)	$S_{\rm core}$ (mJy) (8)	$S_{\rm tot}$ (mJy) (9)	log $L_{1.4}$ (W Hz^{-1}) (10)
J0209+075	6.4 × 5.4	0.12	II	63 ± 4	250 ± 23	121 ± 4	⋯	223 ± 22	25.62 ± 0.10
J0219+015	6.4 × 5.4	0.13	II	39 ± 4	31 ± 3	5 ± 6	⋯	315 ± 31	24.10 ± 0.04
J0802+115	5.4 × 5.4	0.19	II	14 ± 5	41 ± 15	3 ± 23	⋯	21 ± 4	24.24 ± 0.14
J0806+062	5.4 × 5.4	0.17	II	12 ± 4	24 ± 12	73 ± 17	⋯	5.7 ± 2.9	23.27 ± 0.41
J0813+552	5.4 × 5.4	0.16	II	34 ± 4	145 ± 21	54 ± 7	⋯	30 ± 5	24.85 ± 0.13
J0823+033	6.4 × 5.4	0.16	II	⋯	⋯	⋯	16.3 ± 0.5	147 ± 15	24.76 ± 0.09
J0832+184	5.4 × 5.4	0.11	II	14 ± 4	29 ± 8	151 ± 15	⋯	26 ± 4	23.94 ± 0.06
J0833+045	5.4 × 5.4	0.15	II	26 ± 10	101 ± 40	21 ± 23	⋯	25 ± 5	24.65 ± 0.14
J0847+124	5.4 × 5.4	0.16	II	28 ± 3	84 ± 9	4 ± 6	5.1 ± 0.4	7.8 ± 3.3	23.82 ± 0.15
J0855+420	5.4 × 5.4	0.14	I	8.4 ± 2	27 ± 6	38 ± 13	⋯	100 ± 12	25.01 ± 0.13
J0901+164	5.4 × 5.4	0.14	II	43 ± 1	160 ± 13	96 ± 2	⋯	118 ± 12	25.27 ± 0.11
J0903+432	5.4 × 5.4	0.14	II	44 ± 4	229 ± 20	116 ± 5	⋯	7 ± 4	24.51 ± 0.20
J0914+413	5.4 × 5.4	0.18	II	68 ± 10	169 ± 24	172 ± 8	4.7 ± 0.6	374 ± 38	25.29 ± 0.04
J0919+135	5.4 × 5.4	0.20	II	142 ± 7	793 ± 65	160 ± 3	1.8 ± 0.6	233 ± 25	26.14 ± 0.12
J0926+465	5.4 × 5.4	0.14	II	36 ± 2	121 ± 19	155 ± 3	0.5 ± 0.2	11 ± 3	24.11 ± 0.20
J0941+312	5.4 × 5.4	0.15	II	151 ± 7	777 ± 60	53 ± 3	⋯	143 ± 16	25.80 ± 0.11
J0956+162	5.4 × 5.4	0.15	II	37 ± 2	182 ± 23	124 ± 3	5.5 ± 1.0	74 ± 8	25.44 ± 0.18
J0958+561	5.4 × 5.4	0.14	II	92 ± 13	360 ± 55	140 ± 6	6.1 ± 0.5	186 ± 19	25.53 ± 0.09
J1128+241	5.4 × 5.4	0.18	II	53 ± 3	116 ± 19	86 ± 3	⋯	63 ± 8	24.38 ± 0.16
J1136+125	5.4 × 5.4	0.15	II	187 ± 7	127 ± 4	94 ± 2	2.6 ± 0.4	40 ± 7	23.03 ± 0.07
J1303+511	5.4 × 5.4	0.22	II	⋯	⋯	⋯	⋯	174 ± 18	24.83 ± 0.25
J1322+270	5.4 × 5.4	0.16	II	⋯	⋯	⋯	2.9 ± 0.3	2.9 ± 0.3	21.89 ± 0.04
J1328+571	5.4 × 5.4	0.16	II	13 ± 3	8 ± 7	52 ± 12	⋯	17 ± 4	22.61 ± 0.58
J1349+454	5.4 × 5.4	0.15	II	⋯	⋯	⋯	⋯	6.7 ± 0.7	24.18 ± 0.15
J1354+465	5.4 × 5.4	0.16	II	36 ± 3	110 ± 18	94 ± 5	⋯	96 ± 12	24.94 ± 0.17
J1509+515	5.4 × 5.4	0.17	II	23 ± 7	153 ± 46	140 ± 17	⋯	162 ± 16	26.32 ± 0.04
J1633+084	5.4 × 5.4	0.16	II	55 ± 2	227 ± 20	148 ± 2	2.8 ± 0.4	36 ± 6	24.89 ± 0.13
J1636+243	5.4 × 5.4	0.15	II	76 ± 3	163 ± 46	39 ± 2	⋯	61 ± 8	24.34 ± 0.28
J1646+383	5.4 × 5.4	0.16	II	57 ± 11	113 ± 21	140 ± 15	⋯	195 ± 21	24.77 ± 0.04
J1656+640	5.4 × 5.4	0.13	II	150 ± 17	524 ± 59	169 ± 7	0.7 ± 0.2	49 ± 9	24.80 ± 0.07
J1721+262	5.4 × 5.4	0.16	II	224 ± 3	656 ± 8	68 ± 1	2.5 ± 0.6	68 ± 10	24.73 ± 0.06
J2141+082	6.4 × 5.4	0.15	II	9.6 ± 1.0	44 ± 6	13 ± 7	⋯	86 ± 9	25.41 ± 0.14

Note. Col. (1): Object name. Col. (2): Beam size (major×minor axis). Col. (3): Background noise. Col. (4): FR type. Col. (5): Angular distance between the two radio hotspots. Col. (6): Projected proper distance between the two radio hotspots. Col. (7): Position angle of the hotspots relative to the galaxy center, averaged over the hotspot on each side. Col. (8): Flux density of the radio core, if any, measured from two-dimensional Gaussian fits. Col. (9): Integrated flux density of the entire radio source. Col. (10): Absolute luminosity of the entire radio source at 1.4 GHz. Objects J0823+033, J1303+511, J1322+270, and J1349+454 have no well-defined double radio lobes and thus no lobe size and PA measurements.

evolution parameters have large uncertainties, whose precise determination remains controversial (Loveday et al. 2012, 2015; Prescott et al. 2016; Ocran et al. 2021), we conservatively choose to adopt the nonevolutionary results in our analysis.

4. Data Analysis

4.1. Properties of the Radio Core and Lobes

We use CASA to measure the basic radio properties of the sources in the FIRST images (Table 3). We determine the rms noise from the standard deviation of pixel values in the background regions far from the main source. We measure the integrated flux density of the radio lobes and radio core, if present, with polygons that enclose all the radio emission. Provided the redshift of the host galaxy, we infer the absolute radio luminosity $L_{1.4}$ after K-correction assuming a spectral index of -0.8 (Blundell et al. 1999). We fit the hotspots and radio core with a two-dimensional Gaussian profile, respectively, to measure their positions and flux density. We determine the separation between the two hotspots, their mean position angle (PA) relative to the galactic center, and the projected proper distance of the hotspots. We visually classify the radio sources into two types following the precepts of Fanaroff & Riley (1974), according to whether the distance between the two hotspots is smaller than half of the total extent of the double lobes (FR I) or not (FR II).

4.2. Properties of the Host Galaxy

We first estimate and subtract the sky background of the HST images using a sigma-clipping method that iteratively clips the images beyond 3σ, where σ is the standard deviation of the background pixel distribution. We use Photutils to create a segmentation map, setting the segmentation threshold to 2σ above the background noise. The segmentation map allows us to improve the background measurement by calculating the pixel distribution in the sky regions. We create a mask image to remove unrelated sources according to the segmentation map.

With the sky-subtracted image and corresponding segmentation map and mask image, we use the Python package statmorph (Rodriguez-Gomez et al. 2019) to compute

Table 4
Measurement of Host Galaxy Properties of the High-confidence Sample

Name	$m_{\rm tot}$ (mag)	r_e ($''$)	$n_{\rm global}$	ϵ	C	$m_{\rm bulge}$ (mag)	$r_{\rm bulge}$ ($''$)	$\langle\mu_e\rangle_{\rm bulge}$	$n_{\rm bulge}$	PA$_{\rm bulge}$ (°)	$m_{\rm disk}$ (mag)	PA$_{\rm disk}$ (°)	B/T	$\log M_*$ ($M_\odot$)	$g-r$ (mag)
(1)	(2)	(3)	(4)	(5)	(6)	(7)	(8)	(9)	(10)	(11)	(12)	(13)	(14)	(15)	(16)
J0209+075	19.07	2.76	⋯	0.08	3.11	21.26	0.39	19.09	2.23	147	18.96	130	0.11	11.42 ± 0.18	0.86
J0219+015	14.85	12.41	2.01	0.54	3.46	16.03	5.67	20.68	1.31	127	15.16	137	0.31	11.36 ± 0.15	0.84
J0802+115	19.05	1.55	2.18	0.77	4.11	⋯	⋯	⋯	⋯	⋯	⋯	⋯	⋯	10.82 ± 0.20	0.68
J0806+062	18.53	2.94	0.93	0.45	2.66	22.44	0.46	21.41	0.37	165	18.56	155	0.03	9.81 ± 0.52	0.40
J0832+184	17.17	3.12	3.50	0.42	4.53	18.06	1.01	18.70	1.81	18	17.62	164	0.40	11.27 ± 0.15	0.85
J0847+124	18.24	5.85	1.28	0.66	3.00	21.29	1.14	21.92	0.53	56	18.22	115	0.06	11.33 ± 0.15	0.85
J0855+420	19.70	2.04	2.06	0.50	3.17	20.75	1.05	21.12	1.45	2	20.26	173	0.39	11.07 ± 0.20	0.76
J0914+413	16.77	12.00	3.89	0.26	3.24	18.06	2.06	20.16	2.45	5	17.02	27	0.28	11.85 ± 0.15	0.86
J0926+465	19.66	7.30	2.66	0.74	3.32	22.55	0.61	21.69	0.48	68	19.73	68	0.07	10.92 ± 0.25	0.72
J0956+162	20.53	2.21	0.87	0.64	3.08	22.66	0.46	20.43	0.62	167	20.50	23	0.12	10.78 ± 0.25	0.60
J0958+561	19.13	4.76	5.53	0.47	4.35	19.90	0.83	19.45	2.85	91	19.59	95	0.43	11.17 ± 0.17	0.76
J1128+241	18.45	4.16	2.23	0.19	2.93	21.07	0.54	20.35	1.72	3	18.40	50	0.08	10.30 ± 0.23	0.46
J1328+571	16.74	9.42	1.63	0.41	3.27	⋯	⋯	⋯	⋯	⋯	17.09	70	0.00	8.89 ± 1.34	0.20
J1633+084	19.68	3.53	1.66	0.49	2.99	21.86	0.57	20.42	0.37	45	19.64	47	0.11	11.35 ± 0.19	0.85
J1646+383	17.75	2.28	2.76	0.35	3.76	19.63	0.50	18.80	0.16	26	18.06	32	0.19	10.91 ± 0.15	0.72
J1656+640	18.33	4.68	2.13	0.56	3.43	19.91	1.43	20.83	1.08	54	18.50	56	0.21	11.46 ± 0.15	0.70
J1721+262	18.63	3.44	⋯	0.15	4.47	19.45	1.52	20.71	6.24	176	18.29	16	0.34	10.99 ± 0.15	0.78
J2141+082	20.45	2.22	3.19	0.67	3.56	22.61	0.18	18.45	1.41	25	20.60	16	0.14	11.13 ± 0.21	0.53

Note. Col. (1): Object name. Col. (2): Petrosian magnitude after correction for Galactic extinction. Col. (3): Effective radius from fitting a single-Sérsic model. Objects J0209+075 and J1721+262 are not well fit by a single-Sérsic model, and for them we adopt the half-light radii from nonparametric measurements. Col. (4): Global Sérsic index from the single-Sérsic model fit. Col. (5): Ellipticity from nonparametric measurements, defined by $\epsilon = 1 - b/a$. Col. (6): Concentration parameter, defined by $C = 5\log(r_{80}/r_{20})$. Cols. (7)–(13): Magnitude, effective radius, effective surface brightness (R mag arcsec^{-2}), Sérsic index, and position angle (east of north) of the bulge and disk components derived from a two-component Sérsic model. Col. (14): Bulge-to-total luminosity ratio. Col. (15): Stellar mass. Col. (16): Rest-frame $g - r$ color of the entire galaxy. Object J0802+115 is an irregular galaxy without meaningful bulge–disk decomposition, while object J1328+571 is a dwarf (Magellanic spiral) galaxy without a bulge ($B/T = 0$).

several nonparametric quantities of interest (Table 4), including the total magnitude ($m_{\rm tot}$) within the Petrosian (1976) radius, ellipticity $\epsilon \equiv 1 - b/a$, with a the semimajor and b the semiminor axes calculated from the second-order moments,[6] and the concentration parameter $C \equiv 5\log r_{80}/r_{20}$ (Conselice 2003), where r_{80} and r_{20} are the circular aperture radii enclosing 80% and 20% of the total flux, respectively.

We use `GALFIT` to model the two-dimensional light distribution of the galaxy. As in Zhuang & Ho (2022), we construct a point-spread function using `reproject`[7] to stack unsaturated bright stars within the same image of each object. To reproject and stack the stars, we adopt the flux-conserving scheme `spherical polygon intersection`, which treats pixels as four-sided spherical polygons and computes the exact overlap of pixels on the sky. We first fit the galaxy using a single-Sérsic component to obtain a global model, yielding the effective radius r_e and Sérsic index $n_{\rm global}$. We then fit two components to decompose the bulge and disk,[8] using a Sérsic component with a free index $n_{\rm bulge}$ to model the bulge and an exponential profile to model the disk. Obvious dust lanes were masked manually to mitigate their effects on the fits. The model residual images show that in general the two-component bulge–disk decompositions are quite successful. We find no evidence for any additional component that might arise from a prominent nucleus. Figure 3 shows a couple of examples of the decompositions, and the fits for the full set of galaxies can be found in Appendix C. Table 4 summarizes the fitting results, which include quantitative parameters for the bulge and disk. Our fits do not take detailed features such as spiral arms into account. According to Gao & Ho (2017), the systematic uncertainties introduced by this oversimplification are 0.14 mag for $m_{\rm bulge}$, 10% for $r_{\rm bulge}$, and 14% for $n_{\rm bulge}$.

We estimate the stellar mass of the host galaxies using SDSS multiband photometry and the method of Taylor et al. (2011), which is based on the rest-frame i-band absolute magnitude and $g - i$ color of $z < 0.65$ (median z = 0.2) galaxies. The 1σ uncertainty in $\log M_*$ is ~0.1 dex. We use SDSS magnitudes in the g and i bands and apply K-correction (Chilingarian et al. 2010; Chilingarian & Zolotukhin 2012) and Galactic extinction correction to convert to rest-frame magnitudes. The final error budget of the stellar mass has contributions from the redshift, K-correction, and the stellar mass estimation method. Seven objects overlap with the second release of the Galaxy Evolution Explorer–SDSS–WISE Legacy Catalog (GSWLC-2; Salim et al. 2016, 2018), whose stellar masses are derived from ultraviolet-to-infrared SED fitting. Comparing the stellar masses estimated in this paper and those from GSWLC-2, we find good agreement between the two methods, with maximum difference $\Delta\log M_* < 0.3$ dex.

We compare the radio galaxies with normal galaxies in CGS (Ho et al. 2011), a statistically complete sample of 605 bright ($B_T < 12.9$ mag), southern ($\delta < 0°$) galaxies imaged in the optical with the facilities at Las Campanas Observatory. The images have a median seeing of $\sim 1''$, field of view of $8\rlap{.}'9 \times 8\rlap{.}'9$, and median limiting surface brightness ~27.5, 26.9, 26.4, and 25.3 mag arcsec^{-2} in the B, V, R, and I bands, respectively. The flux fraction radii (thus concentration

[6] Equations (24)–(25) from the `SExtractor` user manual at https://readthedocs.org/projects/sextractor/downloads/.

[7] https://reproject.readthedocs.io/en/stable/index.html

[8] Although Zoo Gems also used `GALFIT` to analyze the images, no details were given by Keel et al. (2022).

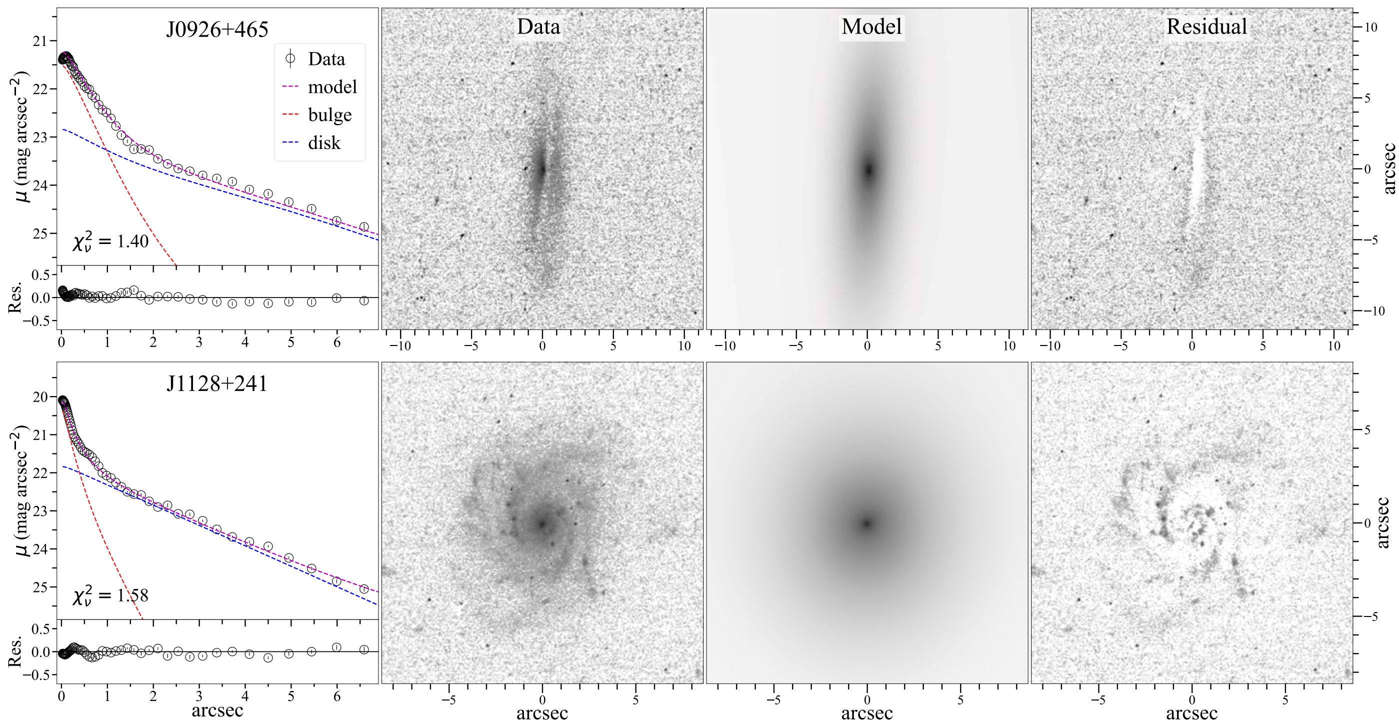

Figure 3. Examples of two-dimensional bulge–disk decomposition using GALFIT. The left column shows the surface brightness profile of the data (open circles with error bars), Sérsic bulge component (red), exponential disk component (blue), and total (bulge + disk) model (purple). The χ^2_ν from GALFIT is shown in the lower-left corner. The lower panel gives the residuals between the data and the model. The right three columns show the original data, best-fit total model, and residuals, respectively. All images are displayed on a log stretch.

parameter) are provided in Li et al. (2011), and Gao et al. (2019) give bulge-to-total light ratios (B/T) and bulge Sérsic indices. We measure the global Sérsic index in the B band with GALFIT, as in Section 4.2. The stellar masses of the CGS galaxies are obtained from modeling with a delayed star formation history using CIGALE (Boquien et al. 2019) their complete optical and near-IR photometry (M.-Y. Zhuang et al. 2022, in preparation), when available, and otherwise from the $B-V$ color and K or I (if K is not available) magnitude using the conversions from Bell et al. (2003). Figure 4 shows the parameter distributions of the radio disk galaxies compared to the control sample of CGS galaxies. Although our galaxies were not observed in the same bands and have slightly higher redshift ($z \approx 0.2$) than the CGS nearby galaxy sample, the difference in structural parameters is expected to be mild (Häußler et al. 2013, 2022; Conselice 2014).

Six galaxies in the high-confidence sample have SDSS spectra, whose spectroscopic fiber covers the central 3″ or ∼2–10 kpc of the galaxies. We obtain emission-line fluxes from the SDSS galSpecLine catalog (Brinchmann et al. 2004). For objects with signal-to-noise ratios larger than 2 for Hβ, [O III] λ5007, Hα, and [N II] λ6584 or [S II] $\lambda\lambda$6716, 6731, we show their Baldwin et al. (1981) diagnostic diagrams in Figure 5. Five objects host AGNs or composite (AGN plus star-forming) nuclei according to the [O III]/Hβ–[N II]/Hα diagram, while in the [O III]/Hβ–[S II]/Hα diagram one object is a Seyfert and two are low-ionization nuclear emission-line regions (LINERs; Heckman 1980). The two LINERs (J0914+413 and J1721+262) both have a compact radio core in their nucleus, a common feature in AGNs with low accretion rates (Ho 2002, 2008).

5. Statistical Properties

5.1. Massive, Quiescent, Disk-dominated Hosts

Radio galaxies mostly consist of giant ellipticals with stellar masses exceeding $10^{11}\,M_\odot$ (Best et al. 2005). The hosts of our sample of double-lobed radio galaxies are also predominantly massive systems (Figure 4), having a median stellar mass $M_* = 1.3 \times 10^{11}\,M_\odot$. As with other massive galaxies in the nearby universe, they have optical colors ($\langle g-r\rangle = 0.69 \pm 0.18$ mag, corrected for redshift and Galactic extinction) that place them on the red sequence (Blanton & Moustakas 2009). There are, however, two noteworthy outliers that have blue colors and unexpectedly low stellar masses: J0806+062 with $M_* = 6.5 \times 10^9\,M_\odot$ and $g-r = 0.4$ mag, and J1328+571 with $M_* = 7.8 \times 10^8\,M_\odot$ and $g-r = 0.13$ mag. The extreme late-type, barred spiral morphology of J1328+571 bears a striking resemblance to the Large Magellanic Cloud, which is only ∼3 times more massive ($M_* = 2.7 \times 10^9\,M_\odot$; van der Marel et al. 2002). Nothing particularly unusual stands out in terms of the effective radii of the sample: most of the members obey the stellar mass–size relation of massive, quiescent galaxies at $z \approx 0.2$–0.4 (Figure 6; Kawinwanichakij et al. 2021).

However, completely counterintuitive to expectation, the galaxies in our sample have stellar morphologies and internal substructures of unmistakably disk-dominated, in many instances extremely late-type galaxies. Even a cursory inspection of the high-quality, optical HST images in Figure 1 reveals that the hosts clearly have disks, as evidenced by spiral structure when viewed at low inclinations and large-scale dust lanes when seen edge-on. Six galaxies (J0209+075, J0806+062, J1128+241, J1328+571, J1646+383, J1656+640) have spiral features, and seven (J0219+015, J0847+124, J0855+420, J0914+413,

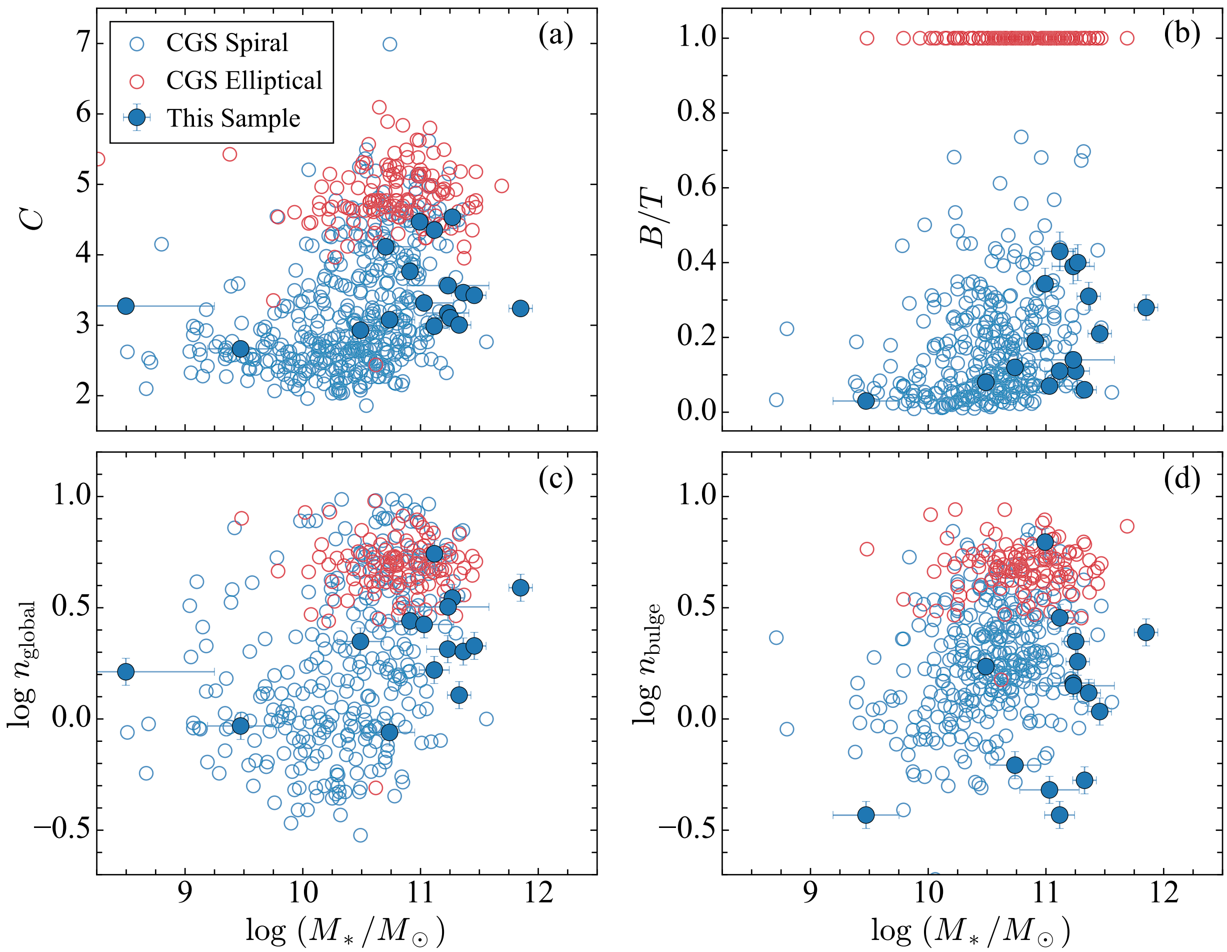

Figure 4. Distribution of (a) concentration parameter C, (b) bulge-to-total light ratio B/T, (c) global Sérsic index $n_{\rm global}$, and (d) bulge Sérsic index $n_{\rm bulge}$ for our sample of disk radio galaxies, in comparison with the control sample of normal galaxies from CGS (blue symbols, spirals; red symbols, ellipticals; Li et al. 2011; Gao et al. 2019). The irregular galaxy J0802+115 and the dwarf Magellanic spiral galaxy J1328+571, which do not have a bulge, are not shown in panels (b) and (d). All quantities pertain to the R band.

J0926+465, J0956+162, J1633+084) have prominent dust lanes with dimensions comparable to that of the entire galaxy, which are common in spiral galaxies and are regarded as signatures of edge-on spiral disks (Holwerda et al. 2019). In sum, we conclude that ∼70% of the sample has spiral arms. The late-type nature of the hosts is further supported by more quantitative metrics. For instance, the sample galaxies have concentrations (median $C = 3.3 \pm 0.5$) consistent with late-type galaxies (Conselice 2014; $C = 3.1 \pm 0.4$), which is further reinforced by their high global ellipticities (median $\epsilon = 0.48 \pm 0.19$) and low Sérsic indices (median $n_{\rm global} = 2.2 \pm 1.2$). Such low values of the optical concentration and global Sérsic index deviate strongly from the majority of $M_* \approx 10^{11} M_\odot$ galaxies (Figures 4(a) and (c)), and elliptical galaxies are rarely flatter than $\epsilon = 0.7$ (Sandage et al. 1970).

An equally remarkable testimony to the exceptionally late-type nature of the host galaxies comes from the bulge-to-disk decomposition analysis described in Section 4.2 (Figure 3; Appendix C), which yields a sample median $B/T = 0.13$. Seven sources have $B/T \lesssim 0.1$ and can be deemed essentially bulgeless. Formally speaking, J1328+571 is truly bulgeless. As a consequence of their different evolutionary histories (Kormendy & Kennicutt 2004; Kormendy & Ho 2013), galactic bulges fall into two types—classical and pseudo—that can be broadly distinguished by their internal kinematics, structure, and radial light profile. Many authors (e.g., Fisher & Drory 2008, 2016) classify bulges according to the value of their Sérsic index: classical and pseudobulges are defined by $n > 2$ and $n \leqslant 2$, respectively. By this criterion, the vast majority (12/16 or 75%) of our sample galaxies with successful bulge-to-disk decomposition qualify as having a pseudobulge, not an unanticipated result in view of the low B/T values that dominate the sample and the tendency for pseudobulges to have $B/T \lesssim 0.35$ (Kormendy & Ho 2013; Kormendy 2016). Others argue, however, that the Sérsic index can yield misleading bulge classifications (e.g., Gadotti 2009; Gao et al. 2018), advocating instead that bulge classification should place greater reliance on the Kormendy (1977) relation between surface brightness and effective radius, to which classical bulges and ellipticals adhere but pseudobulges do not (Neumann et al. 2017; Gao et al. 2020, 2022; Sachdeva et al. 2020). Using the CGS R-band Kormendy relation of ellipticals and classical bulges as a reference, Figure 7 illustrates that the bulges of our sample of disky radio galaxies systematically deviate to lower surface brightness at fixed effective radii, consistent with the expected behavior of pseudobulges (Gao et al. 2020, 2022). To enable this comparison, we K-corrected the HST F475W magnitudes to the R band, assuming a bulge SED from Kinney et al. (1996) and using `Astrolib PySynphot` (STScI Development Team 2013).

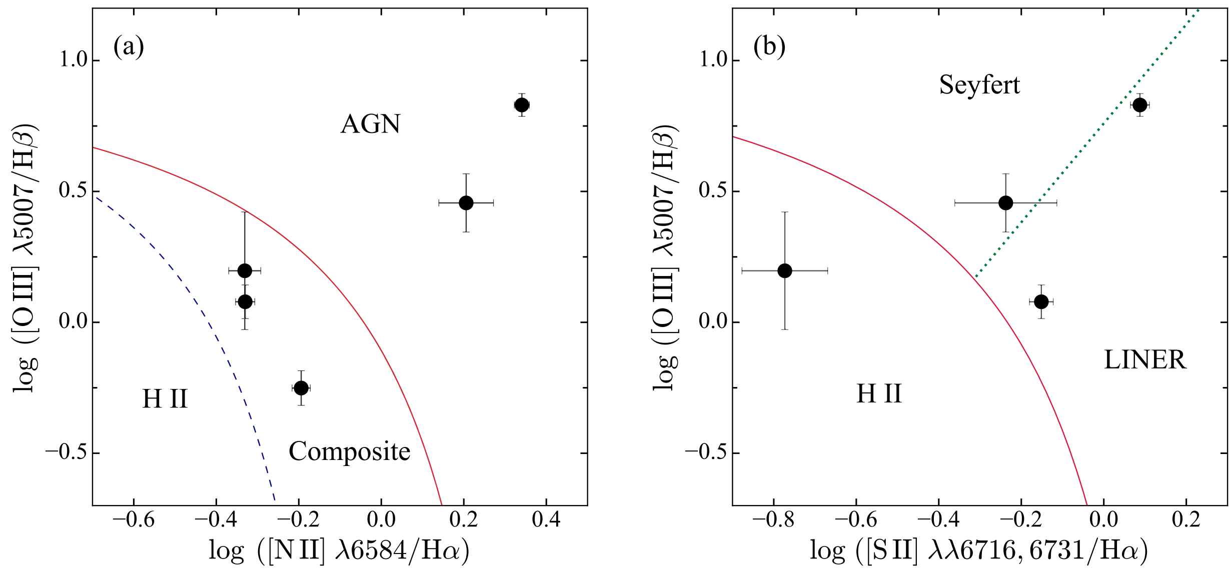

Figure 5. [O III]/Hβ vs. (a) [N II]/Hα and (b) [S II]/Hα diagnostic diagrams for objects with signal-to-noise ratios larger than 2 in their optical emission-line fluxes. The extreme starburst boundary (red solid line; Kewley et al. 2001), the pure star formation line (blue dashed line in panel a; Kauffmann et al. 2003), and the separation between Seyferts and LINERs (green dotted line in panel b; Kewley et al. 2006) are used to classify galaxies into star-forming (H II) galaxies, Seyferts, LINERs, and composite (star-forming and AGN) systems.

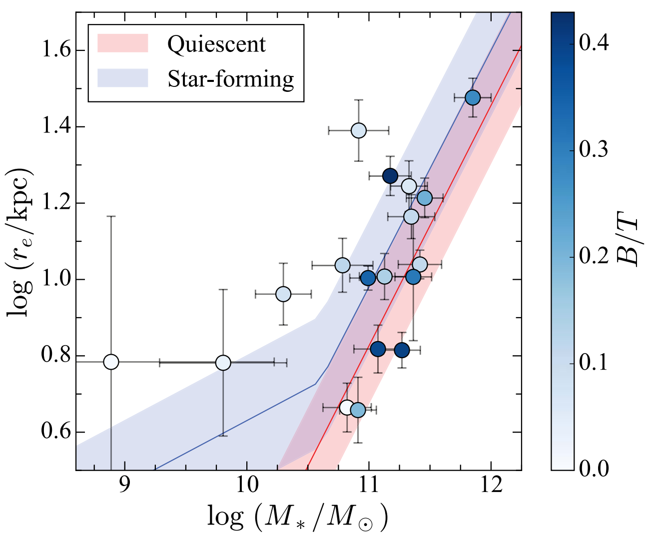

Figure 6. Effective radius (r_e) vs. stellar mass (M_*) for the host galaxies of the double-lobed radio sources in our sample, with colors indicating their bulge-to-total light ratios (B/T). The blue and red solid lines represent the mass–size relations of star-forming and quiescent galaxies at $z \approx 0.2$–0.4 (Kawinwanichakij et al. 2021), with shaded areas indicating the 1σ intrinsic scatter of $\log r_e$.

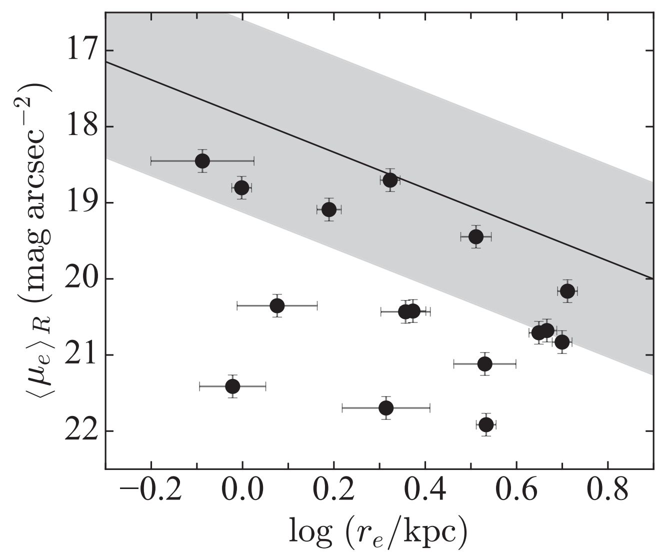

Figure 7. Distribution of bulges of host galaxies in the Kormendy relation. The black solid line shows the Kormendy relation measured in the R band from Gao et al. (2020), with the shaded region showing the 3σ range. Classical bulges and ellipticals follow the Kormendy relation, while pseudobulges are low-surface brightness outliers below the relation. The HST F475W magnitudes have been K-corrected to the R band.

It is quite unusual for spiral galaxies to have stellar masses as large as those in our sample, for the characteristic stellar mass of spiral galaxies is $\sim 3 \times 10^{10}\,M_\odot$, above which the galaxy number density significantly drops (Kelvin et al. 2014; Ogle et al. 2016). Spiral galaxies with $M_* > 10^{11}\,M_\odot$ are extremely uncommon and have been systematically studied only recently (Ogle et al. 2016, 2019). Rarer still are spiral galaxies that host powerful radio AGNs. The large fraction of massive objects in our sample suggests that they are not a random subset of normal galaxies. The nearest neighbors two-sample test (Rizzo 2019), as implemented in the `CRAN` package `yaImpute` (Crookston & Finley 2008), yields p-values <0.02 when we compare their distributions with CGS spiral galaxies in the four diagrams of Figure 4. Prior to this study, nine secure cases of double-lobed radio sources hosted by disk had been reported (Table 5), among which only one (J0315−1906; Keel et al. 2006) had the benefit of high-resolution imaging from HST. Intriguingly, six of the nine cases also have stellar masses $M_* \gtrsim 10^{11}\,M_\odot$. Together with the statistics from our new sample, these trends suggest that the formation of large-scale radio lobes may be linked to the unusually high stellar mass of the hosts. We will revisit this topic in Section 6.

5.2. FR I–FR II Dichotomy

FR II radio sources are on average more powerful than FR I radio sources (Fanaroff & Riley 1974), with the division

Table 5
Double-lobed Radio Sources Hosted by Disk Galaxies from the Literature

Name (1)	R. A. (J2000) (h m s) (2)	Decl. (J2000) (° ′ ″) (3)	z (4)	D (kpc) (5)	$L_{1.4}$ (W Hz^{-1}) (6)	FR Type (7)	M_R (mag) (8)	log M_* ($M_\odot$) (9)	log $M_{\rm BH}$ ($M_\odot$) (10)	References (11)
J0315−1906 (0313−192)	03 15 52.1	−19 06 44	0.067	200	1.0×10^{24}	I	−21.28	10.41	7.31	1
J0354−1340	03 54 32.8	+13 40 07	0.076	240	2.06×10^{23}	II	−21.91	10.66	7.72	2
J0836+0532	08 36 55.9	+05 32 42	0.099	420	1.53×10^{24}	II	−23.11	11.36	8.85	3
J1159+5820	11 59 05.8	+58 20 36	0.054	392	2.26×10^{24}	II	−23.32	11.36	8.85	3
J1352+3126	13 52 17.8	+31 26 46	0.045	335	2.26×10^{25}	II	−22.80	11.32	8.79	3
J1409−0302 (Speca)	14 09 48.8	−03 02 32	0.138	1000	7.0×10^{24}	II	−23.16	11.57	9.19	4
J1649+2635	16 49 23.9	+26 35 03	0.055	86	1.07×10^{24}	II	−22.85	11.42	8.94	3, 5
J2345−0449	23 45 32.7	−04 49 25	0.076	1600	2.5×10^{24}	II	−22.86	11.04	8.33	6
MCG+07−47−10	23 18 32.7	+43 14 49	0.012	207	1.12×10^{22}	II	−20.67	10.16	6.92	7

Note. Col. (1): Object name. Cols. (2)–(3): Coordinates. Col. (4): Redshift. Col. (5): Projected proper distance between the two radio hotspots; for J0354−1340, what is shown is the deprojected linear size. Col. (6): Radio luminosity at 1.4 GHz. Col. (7): FR type. They are predominantly classified as FR II but have much lower radio power than the lower limit of FR II sources hosted by elliptical galaxies (3×10^{25} W Hz^{-1}; Tadhunter 2016). Col. (8): Host galaxy R-band absolute magnitude. For objects J0836+0532, J1159+5820, J1352+3126, J1409−0302, and J1649+2635, we derive the R-band magnitude from the SDSS gri magnitudes according to Jester et al. (2005). For the others with more limited photometry, we derive their R-band magnitude assuming the color of Sab galaxies, following the conversions in Fukugita et al. 1995 and Chilingarian et al. (2017). Col. (9): Stellar mass of the host galaxy, computed as described in Section 4.2. Col. (10): black hole mass, computed from M_* as described in Section 5.2. Col. (11): References: (1) Ledlow et al. (1998); (2) Vietri et al. (2022); (3) Singh et al. (2015); (4) Hota et al. (2011); (5) Mao et al. (2015); (6) Bagchi et al. (2014); (7) Mulcahy et al. (2016).

occurring at a power of $\sim 10^{26}$ W Hz^{-1} at 178 MHz, or, equivalently at 1.4 GHz, $L_{1.4} \approx 3 \times 10^{25}$ W Hz^{-1} (Tadhunter 2016). Owen & Ledlow (1994, see also Ledlow & Owen 1996) suggested that the division line correlates with the absolute magnitude of the host galaxy,

$$\log\left(\frac{L_{1.4}}{\rm W\ Hz^{-1}}\right) = -0.66 M_R + 10.37, \tag{7}$$

where M_R is the Cousins R-band absolute magnitude. Figure 8 shows where our objects lie with respect to the FR I–FR II dichotomy, as defined by the elliptical radio galaxy sample of Owen & Ledlow (1994). We obtain the R-band magnitude of our objects from their SDSS magnitudes, adopting conversions from Jester et al. (2005) with K-correction applied. To maximize the sample, we also add the previously known disk galaxies hosting double-lobed radio sources (Table 5).

Even though all but two of the combined sample of 27 objects have FR II morphologies, nearly all lie below the Owen–Ledlow relation because they tend to have much lower radio power than traditional FR II sources hosted by elliptical galaxies of the same optical luminosity. Violating the well-established FR I–FR II dichotomy, disk radio sources have radio powers characteristic of FR I systems but nevertheless display FR II morphologies. Moreover, the fraction of FR II sources among spiral hosts significantly exceeds that in elliptical radio galaxies, for which the proportion of FR I and FR II types is roughly equal (Capetti et al. 2017a, 2017b). Singh et al. (2015) suggest that the radio lobes hosted by spiral galaxies may be in a late phase of evolution, caught during a period when the radio emission has subsided. However, if radio lobes expand slowly and fade rapidly, as theory predicts (Luo & Sadler 2010), the fading stage lasts but a fleeting moment compared to the lifetime of the jet, rendering the fading scenario implausible to explain the low powers of all disk radio sources discovered to date.

What physically underpins the Owen–Ledlow relation? In view of the fundamental connection between the BH mass and bulge stellar mass (Kormendy & Ho 2013), Ghisellini & Celotti (2001) proposed that the Owen–Ledlow relation ultimately

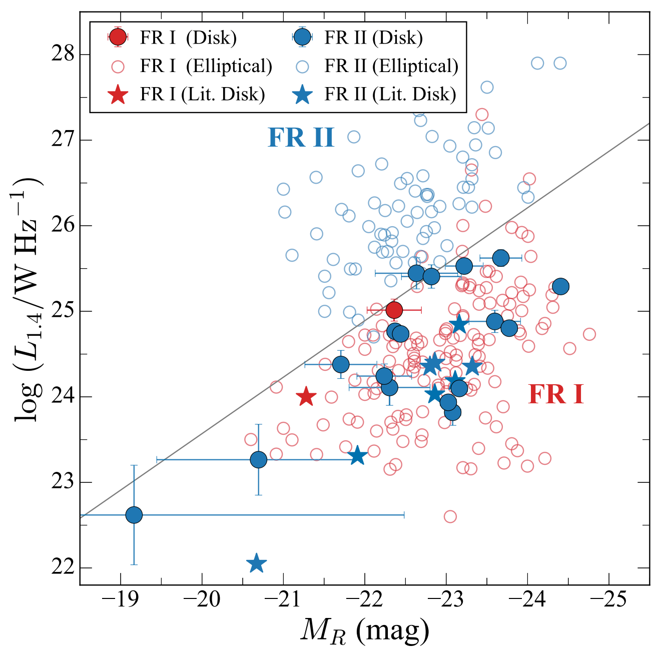

Figure 8. Radio–optical luminosity relation showing the FR I–FR II dichotomy. The solid line is the Owen–Ledlow relation that divides FR I (red) and FR II (blue) sources. Large filled circles are objects from our sample, stars are objects from the literature (Table 5), and small open circles are elliptical galaxies from Owen & Ledlow (1994).

reflects a connection between radio power and the mass of the central BH. To revisit this idea, we estimate the BH masses of our combined sample of spiral hosts (Tables 4 and 5) with the aid of the empirical scaling relation between the BH mass and galaxy total stellar mass (Greene et al. 2020). Note that the slope, zero-point, and intrinsic scatter of the $M_{\rm BH}$–M_* relation vary considerably depending on galaxy morphological type. While the disk-dominated structure of the hosts tempts us to consider the relation for late-type galaxies, we are conflicted simultaneously by the large stellar masses of the hosts that more closely mimic early-type galaxies. For concreteness, we

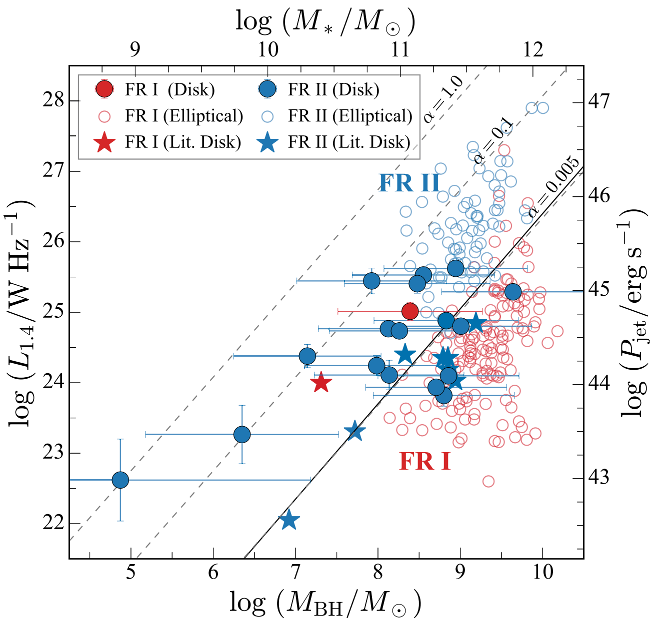

Figure 9. Radio luminosity–BH mass relation showing the FR I–FR II dichotomy. The top x-axis gives the total stellar mass. The right y-axis converts radio luminosity to jet power following Equation (10). The solid line is the BH mass version of the Owen–Ledlow relation, where we converted the R-band absolute magnitude to BH mass as described in Section 5.2. The dashed lines show constant critical ratios of jet power over Eddington luminosity, $\alpha \equiv P_{\rm jet}/L_{\rm Edd} = 1$, 0.1, and 0.005. Large filled circles are objects from our sample, stars are objects from the literature (Table 5), and small open circles are elliptical galaxies from Owen & Ledlow (1994).

choose the relation calibrated using all galaxy types combined:

$$\log\left(\frac{M_{\rm BH}}{M_\odot}\right) = (7.43 \pm 0.09) + (1.61 \pm 0.12)\log\left(\frac{M_*}{M_0}\right), \quad (8)$$

with $M_0 = 3 \times 10^{10}\,M_\odot$ and an intrinsic scatter of 0.81 dex. At a fiducial stellar mass of $M_* = 10^{11}\,M_\odot$, the scaling relation of early-type galaxies overpredicts $M_{\rm BH}$ by 0.36 dex, while the late-type galaxy calibration underpredicts $M_{\rm BH}$ by 0.69 dex. We are even warier of relying on scaling relations based on the bulge properties, in view of the poor link between BHs and pseudobulges (Kormendy & Ho 2013). Figure 9 shows the Owen–Ledlow relation transformed into the reference frame of the BH mass,

$$\log\left(\frac{L_{1.4}}{\mathrm{W\ Hz^{-1}}}\right) = 1.35\log\left(\frac{M_{\rm BH}}{M_\odot}\right) + 12.9, \quad (9)$$

where we have converted the R-band absolute magnitude to BH mass using the tight (scatter 0.30 dex) correlation between the BH mass and K-band luminosity and $V-K=3.0$ mag (Kormendy & Ho 2013), together with $V-R=0.61$ mag appropriate for ellipticals (Fukugita et al. 1995).

In the new diagram comparing the radio luminosity to the BH mass, the FR I–FR II dichotomy is largely restored, although the introduction of the spiral hosts blurs the sharp boundary between the two types of radio sources as traditionally defined by elliptical hosts. It is possible that the FR I–FR II boundary depends on the morphological type, such that for a given BH mass spiral hosts generate systematically less radio power than their elliptical host counterparts. This can explain the paucity of FR I sources currently found among the new population of spiral hosts. The average radio power of FR Is is ∼2 orders of magnitude weaker than that of FR IIs. Given the typical flux density of 50 mJy of the FR IIs currently detected in disk galaxies, all else being equal to the FR I counterparts would have flux densities of merely 0.5 mJy, which would place them below the detection limit of FIRST, which is 1 mJy for individual sources and even worse for extended radio lobes (Becker et al. 1995). Deeper, higher-resolution observations may yet reveal a more extensive population of FR I sources hosted in spiral galaxies. Indeed, McCaffrey et al. (2022) detected complex, subgalactic radio structures in radio-quiet quasars that are possibly FR I radio lobes, although little is known about the properties of the host galaxies.

Ghisellini & Celotti (2001) suggested that the division between the two types of radio sources may be associated with a transition in the accretion mode, from a radiatively inefficient, advection-dominated accretion flow (Narayan & Yi 1994) in FR Is to the standard geometrically thin, optically thick accretion disk (Shakura & Sunyaev 1973) in FR IIs. The transition occurs at a critical ratio $\alpha \equiv P_{\rm jet}/L_{\rm Edd} \approx 10^{-3}$–$10^{-2}$, where the Eddington luminosity of the BH $L_{\rm Edd} \equiv 1.3 \times 10^{38}(M_{\rm BH}/M_\odot)\,\mathrm{erg\ s^{-1}}$ and jet power (Cavagnolo et al. 2010)

$$\log\left(\frac{P_{\rm jet}}{P_1}\right) = (0.75 \pm 0.14)\log\left(\frac{P_{\rm radio}}{P_2}\right) + (1.91 \pm 0.18), \quad (10)$$

with $P_1 = 10^{42}\,\mathrm{erg\ s^{-1}}$, $P_2 = 10^{40}\,\mathrm{erg\ s^{-1}}$, $P_{\rm radio} \equiv \nu L_\nu$, and $\nu = 1.4$ GHz. Figure 9 shows that the traditional FR I–FR II dichotomy of elliptical hosts corresponds to $\alpha \approx 0.005$, consistent with the notion that the FR dichotomy arises from the transition of accretion modes. If a similar dichotomy exists in disk galaxies, we speculate that it would occur at an even lower value of α. We note that the FR dichotomy in disk radio galaxies appears less distinct than that for the elliptical galaxies from Owen & Ledlow (1994). We suspect that this is partly because our sample, owing to detection limits, lacks FR I objects with low radio luminosities. It is also possible that the dichotomy is intrinsically not sharp and breaks down at low radio power (Best & Heckman 2012; Whittam et al. 2022) as the original Owen & Ledlow (1994) sample is affected by the Malmquist bias.

5.3. Misalignment Between Radio and Optical Axes

It has long been realized that the orientation of radio lobes is not preferentially aligned with the minor axis of elliptical galaxies (Birkinshaw & Davies 1985). Browne & Battye (2010) found that the alignment is related to the ratio of radio to optical flux, with a higher probability of finding alignment in objects with lower ratios. Adopting their classification criterion, all our sources fall in the high-ratio class. The relative position angles (ΔPA) between radio lobes and the minor axis of galactic disks and bulges span a broad distribution, with lobes ranging from aligned (0°) to nearly perpendicular (90°) relative to the galaxy (Figure 10). Notwithstanding a slight, apparent trend toward alignment directions, after accounting for measurement uncertainties and Poisson noise the distribution of ΔPA is still consistent with being uniform, with $\chi^2 = 1.2$ for the disk (Figure 10(a)) and $\chi^2 = 1.4$ for the bulge (Figure 10(b)). As the orientation of the jet is coupled with the spin of the central BH

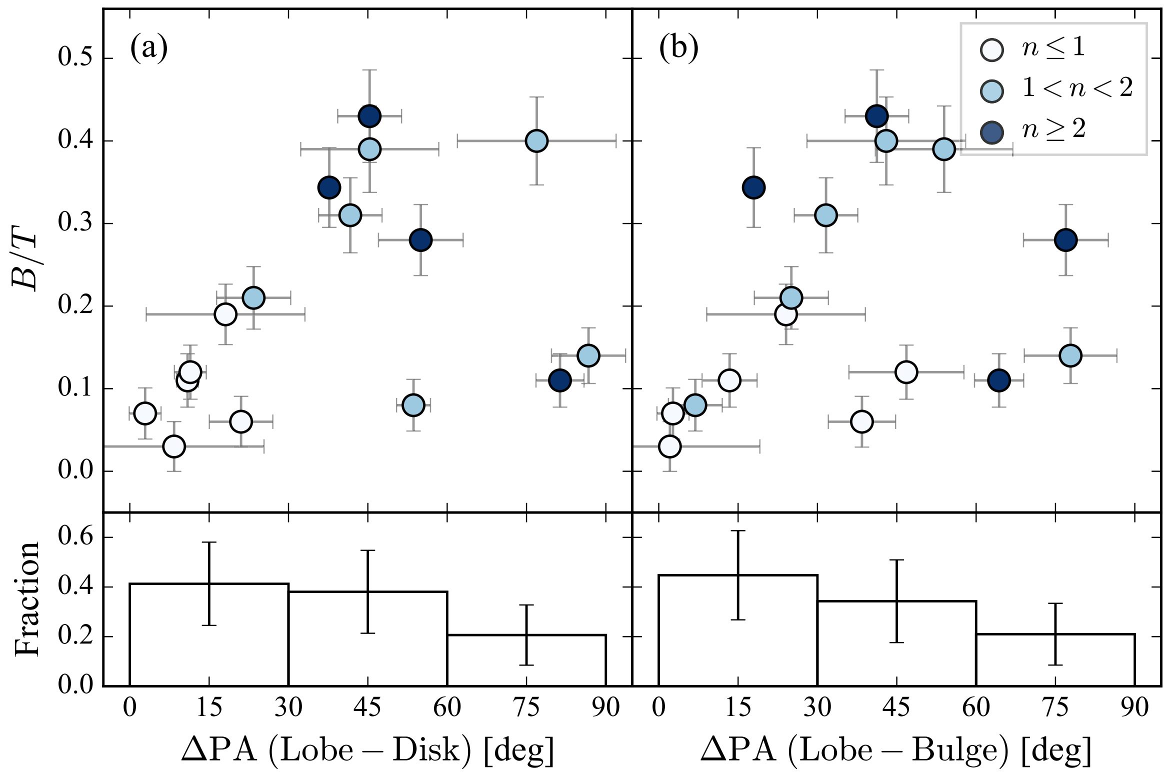

Figure 10. Relative position angle (ΔPA) between the radio lobes and the minor axes of the host galaxy (a) disk and (b) bulge. The upper panels show the correlation between ΔPA and bulge-to-total ratio (B/T), where the color code indicates the bulge Sérsic index (n). The lower panels give the distribution of ΔPA in bins of 30°.

(Blandford & Znajek 1977; Mirabel & Rodríguez 1999), our results suggest that the spin of the BH is not necessarily aligned with the large-scale angular momentum of the host galaxy.

Although ΔPA is randomly distributed for the whole sample, it appears to be mildly correlated with bulge prominence or the bulge type. Host galaxies with the least conspicuous ($B/T < 0.2$), low-Sérsic-index ($n \leqslant 1$) bulges have radio jets that tend to show alignment with the disk and bulge minor axis. In other words, the spin of the central BH of galaxies that evolved secularly through internal gas inflows instead of via mergers may bear the imprint of the angular momentum of the large-scale disk.

6. Discussion

Although historically double-lobed radio sources have been found exclusively in giant elliptical galaxies (Best et al. 2005), to date no clear consensus exists as to how such an association arises. Wilson & Colbert (1995) posited that the galaxy–galaxy mergers that are classically invoked to form ellipticals (e.g., Toomre & Toomre 1972) may also be conducive to spinning up the central BH, a prerequisite for producing strong radio jets if they are powered by the BH spin (Blandford & Znajek 1977). This popular explanation has lost some persuasion, however, because rapidly spinning BHs can evidently inhabit galaxies of diverse morphological types, not only ellipticals (Reynolds 2021).

This study adds a new twist to the narrative. Analyzing HST images acquired as part of the Zoo Gems project (Keel et al. 2022), we demonstrate unambiguously that at least some double-lobed radio sources can originate from late-type galaxies. Unlike previous reports of a similar nature that were largely based on heterogeneous ground-based images (as summarized in Section 1), the evidence introduced here is incontrovertible because of the benefits afforded by high-resolution HST images of uniform quality. Besides having been systematically selected (Banfield et al. 2015), our final high-confidence sample is twice as large as all previously studied cases of a similar nature combined (Table 5). Our quantitative analysis firmly establishes the late-type morphology of the host galaxies through multiple lines of evidence, including the direct detection of spiral arms, large-scale dust lanes, which are likely edge-on projections of spiral arms, high ellipticity, low global Sérsic index, low concentration, and of course low bulge-to-total ratio. The bulges are not merely modest, but, judging from their low Sérsic indices and low effective surface brightnesses relative to the Kormendy relation, they can be categorized as pseudobulges, not classical bulges. These characteristics are extraordinary, but not unprecedented, for the hosts of extended radio sources. The closest analog is J2345−0449, a galaxy with a spectacular 1.6 Mpc scale “double-double” radio jet that hosts a pseudobulge ($n_{\rm bulge} \approx 1$) with $B/T \approx 0.14$–0.18 (Bagchi et al. 2014). Singh et al. (2015) suppose that radio galaxies with late-type optical morphology may originate from ellipticals that recently acquired a disk component after merging with a disk galaxy. We do not believe that this explanation is viable. An elliptical galaxy that swallows a gas-rich companion—the nearby example of Centaurus A comes to mind (Baade & Minkowski 1954; Graham 1979)—can gain a disk, but it cannot lose a gigantic bulge. The sources discussed in this study, which, unlike the majority of previous examples in the literature, have highly robust morphologies and structural parameters derived from high-quality HST images, decidedly do *not* have a substantial classical bulge component.

The unusual nature of the abovementioned characteristics becomes even more acute when we consider the fact that the majority of the spiral hosts have very large stellar masses. More than 60% (11/18) of our main HST sample has $M_* \gtrsim 10^{11}\,M_\odot$, and within the literature sample, the percentage is similar (56% or 5/9; Table 5). Curiously, despite the clear presence of spiral structure in their disks,[9] the optical colors are consistent with those of passive galaxies on the red sequence (Blanton & Moustakas 2009). The subset of galaxies with $M_* \gtrsim 10^{11}\,M_\odot$ has a median optical color, corrected for redshift and Galactic extinction, of $g - r = 0.84$ mag for the HST sample and $g - r = 0.73$ mag for the literature sample. This population of supermassive spiral galaxies is qualitatively reminiscent of the superluminous spirals and lenticulars highlighted by Ogle et al. (2016, 2019). Extremely massive disk galaxies in the nearby universe may have arisen from gas-rich minor mergers (Jackson et al. 2022), or perhaps from having experienced an anomalously quiet merger history (Jackson et al. 2020; Zeng et al. 2021).

If galaxy morphology no longer can be regarded as a unique signpost of a galaxy's ability to generate large-scale radio jets, then what physical parameter is responsible? The key factor seems to be the galaxy's stellar mass, or, equivalently, the BH mass, to the extent that the two are closely related (Equation (9)). Notwithstanding a few outliers (see below), the vast majority of the radio galaxies have stellar masses $\gtrsim 10^{11}\,M_\odot$ or BH masses $\gtrsim 10^{8}\,M_\odot$. This is a long-standing, familiar result in the context of the standard paradigm that radio galaxies are exclusively ellipticals (Dunlop et al. 2003; McLure et al. 2004; Best et al. 2005). The results of this study show that this traditional view must be modified. The hosts of double-lobed radio sources encompass not only elliptical galaxies but also a rare population of spiral/disk galaxies, whose common characteristic is that they, too, have unusually large stellar masses (Figure 9). Of course, not all massive galaxies produce extended radio lobes, but the probability that they do increases with the galaxy stellar luminosity or mass (Scarpa & Urry 2001; Best et al. 2005). As a class, radio-loud AGNs are predominantly hosted by massive galaxies (Mauch & Sadler 2007). Moreover, among the massive galaxies that launch large-scale radio lobes, their radio luminosity or jet power scales roughly with the galaxy stellar mass (Figure 9), which was already implicit in the Owen–Ledlow relation (Figure 8). Combining Equations (9) and (10), we note that the jet power is almost exactly linearly proportional to the BH mass: $P_{\rm jet} \propto M_{\rm BH}^{1}$. Again, we now know that these trends hold irrespective of galaxy morphology. So, too, can be said of the FR I–FR II dichotomy, except that in disk galaxies the transition between the two FR types may occur at a lower value of the critical ratio (α) between jet power and Eddington luminosity. This remains to be verified with future, deeper observations capable of detecting the expected weaker emission of FR I sources.

If the stellar mass—and, by extension, the BH mass—is the primary factor that determines the probability that a galaxy launches radio jets, while, at the same time, it also controls the power of the jet that ultimately gets launched, then perhaps we can understand why extended jet structures are so rarely found in spiral galaxies. The stellar mass function of disk-dominated galaxies is weighted toward substantially lower masses than that of bulge-dominated galaxies, and even more so still when compared to that of ellipticals (e.g., Moffett et al. 2016). Thus, extended radio jets are a priori expected to be both rare and weak in spiral galaxies. Even when present, the jets will be more compact, as the jet size correlates with the jet power (e.g., Ledlow et al. 2002). If the jet does not extend significantly beyond the boundaries of the stellar disk, it is likely to be confused with the native synchrotron emission from star formation. For example, the AGN components of the radio emission in nearby Seyfert galaxies have 1.4 GHz powers $\lesssim 10^{23}$ W Hz^{-1} and linear source sizes $\lesssim$10 kpc (Ho & Ulvestad 2001; Ulvestad & Ho 2001).

We close with some cautionary notes and suggestions for future work. Our study hinges on the key assumption that we have identified the correct optical counterpart of the host galaxy of the radio lobes. While we have devoted concerted efforts to cull a sample for which spurious chance alignment is low (Section 3), of course, such statistical arguments cannot completely guarantee that all the associations are real. Two sources in our sample stand out as glaring outliers. As discussed in Section 5.1, J0806+062 has a stellar mass of only $M_* = 6.5 \times 10^{9}\,M_\odot$, and J1328+571 with $M_* = 7.8 \times 10^{8}\,M_\odot$ is more extreme still. Low-mass galaxies can host nuclear central BHs (Filippenko & Ho 2003; Greene & Ho 2004; Greene et al. 2020), and a minority even have radio cores and compact jets (e.g., Greene et al. 2006; Wrobel & Ho 2006) but not classical double-lobed radio structures. Although J0806+062 and J1328+571 have the lowest radio powers in the sample ($L_{1.4} = 2 \times 10^{23}$ and 4×10^{22} W Hz^{-1}), their radio sources, while also small compared to the rest ($D = 24$ and 8 kpc), are clearly not confined to the nucleus (Figure 1). Follow-up observations are urgently needed to verify the reality of these two baffling sources.

The preceding discussion often presupposes that the BH mass truly traces the galaxy stellar mass. While this has been established for nearby inactive galaxies for which the BH mass can be measured by dynamical methods and for active galaxies for which the BH mass can be estimated through their broad emission lines (see reviews in Kormendy & Ho 2013; Greene et al. 2020), we acknowledge the inherent uncertainty and ambiguity of applying the $M_{\rm BH}$–M_* relation to our sample. Which $M_{\rm BH}$–host galaxy scaling relation, if any, is appropriate for these unusual galaxies? An important next step should secure more complete and higher quality optical spectra of the candidate optical counterparts, to fully delineate the ionization source of their nuclei. Are they all AGNs? If so, what type? X-ray observations (e.g., Mirakhor et al. 2021) would be particularly helpful to disentangle possible confusion arising from dust obscuration or contamination by stellar energy sources. The present sample was originally selected from the FIRST survey, whose sensitivity (∼1 mJy) and angular resolution (∼5″) can be vastly improved with follow-up observations with the Jansky Very Large Array.

7. Summary

We report the existence of disk galaxies as hosts of double-lobed radio sources, using high-resolution optical (F475W) HST images acquired as part of the Zoo Gems program, which targeted 32 sources originally selected from the Radio Galaxy Zoo project that identified double-lobed radio sources associated with disk galaxies from crossmatching the FIRST survey and SDSS. To examine the fidelity and reliability of the physical association between the apparent optical counterparts and radio lobes, we systematically calculate the probability of

[9] This is true at least for the main Zoo Gems sample, which enjoys the benefits of HST imaging that the literature sample, apart from 0313 − 192 (Keel et al. 2006), does not.

chance alignment. For a subset of 18 high-confidence objects for which chance alignment is unlikely, we derive the optical morphologies and global and bulge structural parameters, which are combined with the physical properties of the host and radio sources to understand the nature of jet production.

Our main results are as follows:

1. The host galaxies have unambiguous disk-dominated morphologies, as judged by the presence of spiral arms, large-scale dust lanes among the edge-on systems, and low global Sérsic indices and optical concentrations. Two-dimensional image decomposition yields bulge-to-total light ratios of $B/T = 0$–0.43, with a median value of 0.13. The bulges have low Sérsic indices (median $n_{\rm bulge} = 1.4$) and low effective surface brightnesses that are consistent with pseudobulges.
2. Despite the obvious morphological and structural properties of late-type galaxies, the majority of the hosts have very large stellar masses (median $M_* = 1.3 \times 10^{11}\, M_\odot$) and red optical colors (median $g - r = 0.69$ mag), consistent with massive, quiescent galaxies on the red sequence. A literature sample of nine radio sources previously found to be hosted by disk galaxies shares strikingly similar characteristics.
3. As with the dominant population of elliptical radio galaxies, among disk radio galaxies the jet power scales with the stellar mass. In terms of the black hole mass, $P_{\rm jet} \propto M_{\rm BH}^{1}$.
4. Elliptical radio galaxies display a dichotomy in the $P_{\rm jet} - M_{\rm BH}$ plane, such that sources with an FR II radio morphology produce systematically more powerful jets than FR I sources of the same black hole mass. The separation line corresponds to $P_{\rm jet}/L_{\rm Edd} \approx 0.005$, which may be related to a transition in the accretion mode from a standard disk to a radiatively inefficient accretion flow. Nearly all of the currently known disk radio galaxies are FR II sources. We suggest that among the new population of disky hosts the critical threshold for the accretion mode transition occurs at a lower value of $P_{\rm jet}/L_{\rm Edd}$, which has yet to be reached by the sensitivity of the current radio observations.
5. The axis of the radio jets is uncorrelated with the minor axis of the host galaxy or its bulge, although galaxies with the smallest bulges ($B/T < 0.2$, $n_{\rm bulge} \leqslant 1$) may show a mild preference to be aligned with the jet, suggesting that the angular momentum on nuclear scales bears the imprint of the angular momentum of the large-scale galactic disk, plausibly as a consequence of gas inflows through secular evolution.

We are grateful to the anonymous referee for helpful comments. We thank Subo Dong and Kejia Lee for helpful discussions, and Hua Gao for advice on CGS data. We received financial support from the National Science Foundation of China (11721303, 11991052, 12192220, 12192222, 12011540375) and the China Manned Space Project (CMS-CSST-2021-A04, CMS-CSST-2021-A06). This research is based on observations (program 15445) made with the NASA/ESA Hubble Space Telescope obtained from the Space Telescope Science Institute, which is operated by the Association of Universities for Research in Astronomy, Inc., under NASA contract NAS 526555. We made use of the NASA/IPAC Infrared Science Archive, which is funded by the National Aeronautics and Space Administration and operated by the California Institute of Technology.

Software: `Astrolib PySynphot` (STScI Development Team 2013), `Astropy` (Astropy Collaboration et al. 2018, 2013), `CASA` (McMullin et al. 2007), `GALFIT` (Peng et al. 2002, 2010), `Numpy` (Harris et al. 2020), `Photutils` (Bradley et al. 2020), `reproject` (https://reproject.readthedocs.io/en/stable/index.html), `yaImpute` (Crookston & Finley 2008).

Appendix A
Images of the Low-confidence Sample

We present the images of the low-confidence sample in Figure A1. The radio lobes and optical galaxies have a considerable probability of being chance-aligned, given the large offsets between galaxies and radio centers. However, some may also have genuine associations because our probability estimation of chance alignment is conservative. Moreover, we have not exploited every piece of information to constrain the probabilities. Future observations, including optical spectroscopy, X-ray observations, and radio observations of higher angular resolution and better sensitivity are needed to confirm their associations.

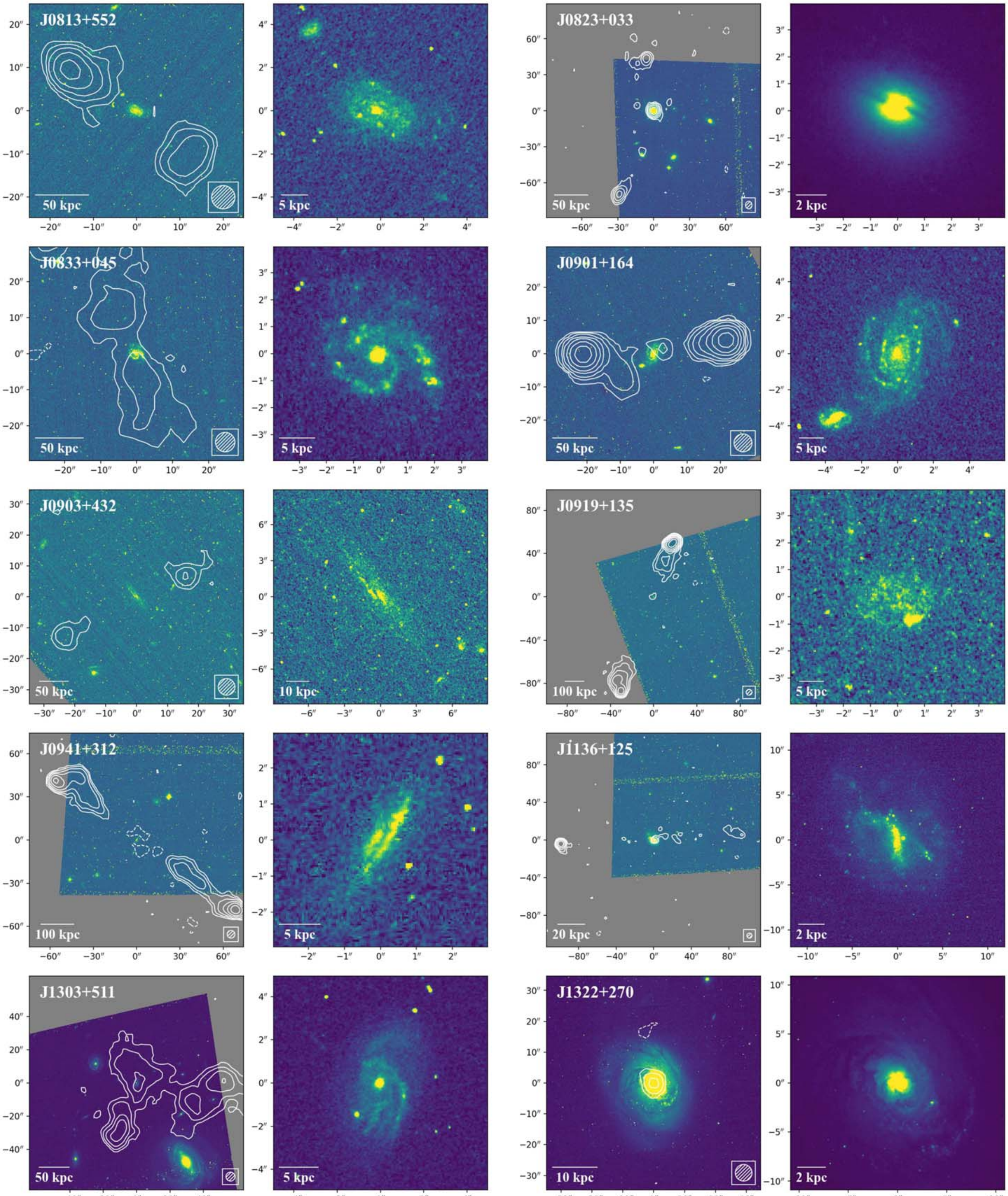

Figure A1. HST F475W images of the 14 low-confidence sources in our sample, overlaid with FIRST 1.4 GHz contours in the left panel and zoomed-in to highlight the optical morphology of the galaxy in the right panel. All images are centered on the galaxy with north up and east to the left. The restoring beam of the radio map is depicted as a hatched ellipse on the lower-right corner. The radio contours are $(-3, 3, 6, 12, 24, 48, 96, ...) \times$rms of each image, where the values of the rms are listed in Table 3. The scale bar in the lower-left corner of each panel indicates the proper distance at the redshift of each object.

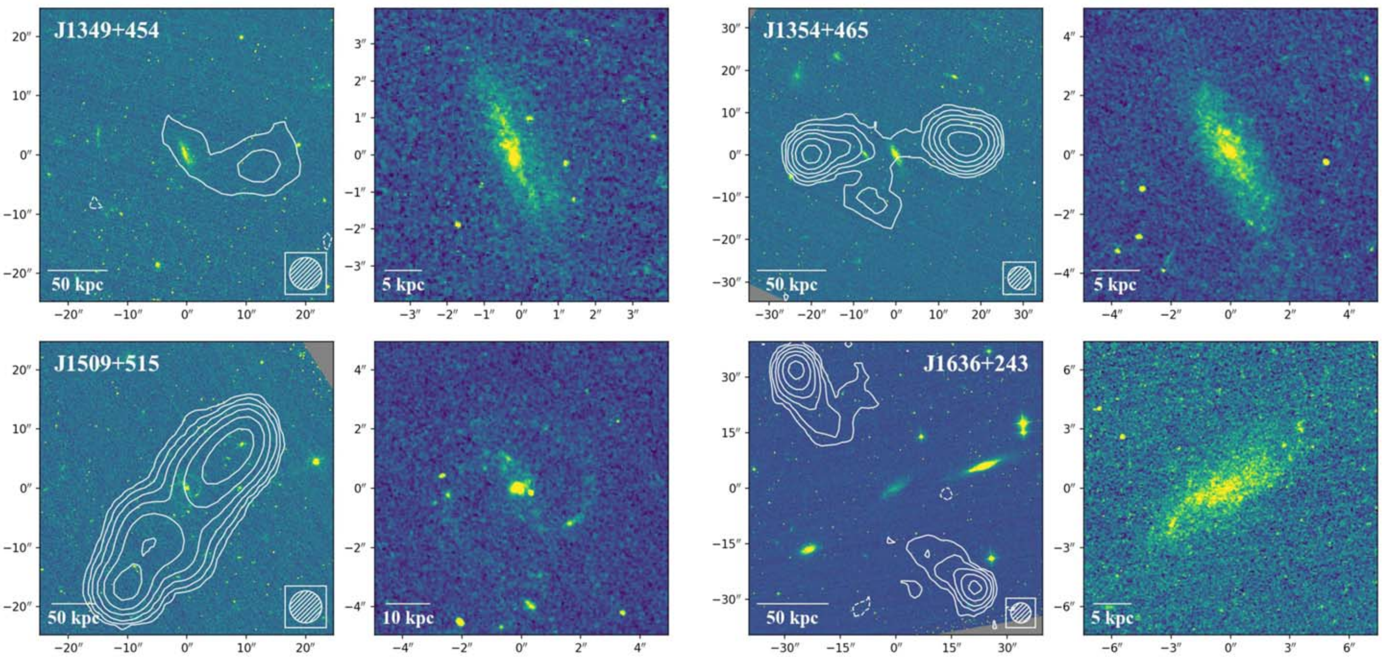

Figure A1. (Continued.)

Appendix B
Notes on Individual Sources

J0209+075: This is a face-on galaxy with a luminous bulge and loose spiral arms, which harbor several star-forming clumps. The southwestern arm looks disjoint from the galaxy, indicating a low stellar density in the inter-arm region. The bright point-like source northwest of the galaxy is a foreground star identified by the SDSS.

J0219+015: This local ($z_{\rm spec} = 0.04$) galaxy has a fairly prominent bulge and prominent dust structures. The radio source is classified as winged or X-shaped (Yang et al. 2019).

J0802+115: We do not attempt to decompose this interacting system, which has an asymmetric light distribution and long tidal tails.

J0806+062: This galaxy shows several spiral arms and a luminous bar-like region. A galaxy to the northeast with $z_{\rm phot} = 0.11 \pm 0.08$ might be a genuine companion. A star to the east of the galaxy with $m_g = 20.7$ mag has been identified by the SDSS and Gaia[10] (Gaia Collaboration et al. 2021).

J0813+552: We assigned the galaxy to the low-confidence sample because it is too faint ($m_g = 20.4$ mag), and the number density at that magnitude is large. In addition, we detect a few sources to the north of the galaxy that might be candidates for the host.

J0823+033: This is a complicated case because the double radio lobes have a wide opening angle relative to the galaxy. Our chance alignment analysis is invalid for this complicated object, and thus we cannot confidently determine the association between the galaxy and the radio lobes.

J0832+184: This galaxy has one of the most prominent bulges in our sample ($B/T = 0.4$), and it exhibits a large degree of lopsidedness, suggesting possible signs of interactions. The northern radio lobe is much brighter than the southern one.

J0833+045: This object has a high probability of chance alignment because the galaxy is faint and off-center from the radio lobes.

J0847+124: This nearly edge-on galaxy has a long dust lane with complicated substructures. The double radio lobes are asymmetric; while the northern lobe is luminous, the southern one is only barely detected. A radio core coincides with the galaxy.

J0855+420: This edge-on late-type galaxy, bisected by a prominent, ∼10 kpc dust lane, has a large stellar mass ($M_* = 1.2 \times 10^{11}\, M_\odot$). The radio structure has an FR I morphology because the hotspots are much closer to the galaxy than the lobes. The double lobes have a total length of ∼400 kpc and a width of ∼100 kpc (projected). The lobes have sinuous shapes near the hotspots.

J0901+164: A massive spiral with $M_* = 8 \times 10^{10}\, M_\odot$, this galaxy has prominent arms and star-forming clumps. The eastern radio lobe has a tail to the southwest instead of toward the direction of the other radio lobe. We crossmatched the peak coordinate of the tail with the AllWISE catalog (Wright et al. 2010) but found no source. A spiral galaxy with $z_{\rm phot} = 0.22 \pm 0.05$ and a prominent bar is located southeast of the main object. Another faint object with $z_{\rm phot} = 1.35 \pm 0.25$ is located to the northwest of the main object and close to the center of the radio contours. To obtain a conservative estimate of the chance alignment probability, we regard this faint object as a possible radio source.

J0903+432: This is a faint ($m_g = 20.7$ mag), very massive ($M_* = 2 \times 10^{11}\, M_\odot$), edge-on galaxy with a prominent dust lane. The radio lobes are perpendicular to the galaxy plane. It has a high probability of being chance-aligned with the radio lobes because the number density of galaxies of this magnitude is large.

J0914+413: The galaxy is bisected by a prominent, ∼10 kpc dust lane. The complicated dust lane introduces significant uncertainties to the bulge-to-disk decomposition. The northern

[10] https://irsa.ipac.caltech.edu/cgi-bin/Gator/nph-dd

lobe has a second peak with an intensity half of that of the main one, but no counterpart is found in the HST image and AllWISE catalog. In addition to the two lobes, a radio core coincides with the galaxy.

J0919+135: This is likely a chance-aligned case because the galaxy is too faint (m_g = 21.5 mag) and significantly offset from the center of the radio lobes ($r_{\rm offset} = 18\farcs1$). Moreover, many other objects are detected near the center of the radio lobes that may be candidate hosts.

J0926+465: This is an edge-on galaxy with a dust lane ∼20 kpc long. In addition to the two lobes, faint radio emission also coincides with the galaxy.

J0941+312: We classified this faint edge-on galaxy as a low-confidence object. However, it is located in the center of radio emission, and no other sources are detected nearby. The radio lobes have an angular size of $\sim 2\farcm5$. If they are associated with the galaxy, which has $z_{\rm phot} = 0.366 \pm 0.037$, the physical dimension would be ∼1.4 Mpc, similar to J2345−0449 (Bagchi et al. 2014).

J0956+162: This edge-on galaxy with a prominent (∼15 kpc) dust lane has intense radio emission from the nucleus, with peak intensity reaching $\sim 1.1\ {\rm mJy\ beam^{-1}}$. The two radio lobes are roughly equidistant from the center of the galaxy. We find an object with $z_{\rm phot} = 0.46 \pm 0.08$ in the direction of the eastern lobe, $\sim 2''$ offset from the radio peak; it is unlikely to be associated with the radio lobe because of its small size ($0\farcs91 \pm 0\farcs04$) and faintness ($m_{\rm F475W} = 22.5 \pm 0.1$ mag).

J0958+561: The galaxy has a prominent bulge and an extended disk. Its nuclear region is complicated in the HST image. The GALFIT residuals reveal a compact source near the center, which might be a candidate secondary nucleus (see Figure C1). In addition to the two lobes, a radio core coincides with the galaxy.

J1128+241: This is a nearly face-on spiral galaxy with obvious star-forming clumps along its arms, rendering its optical color ($g - r = 0.46$ mag) bluer than those of others in the sample.

J1136+125: This is a low-mass galaxy ($M_* = 2 \times 10^9\, M_\odot$) with a peculiar morphology and distortions in its outer regions. It has a star formation rate of $0.4\, M_\odot\, {\rm yr}^{-1}$ according to GSWLC-2. We do not consider it a likely host for the radio source. We note that there is a bright point source with $m_{\rm F475W}$ = 22.1 mag located only $1''$ west of the galactic center, which should be investigated further as a possible quasar candidate responsible for the radio lobes.

J1303+511: The radio morphology is too complicated to interpret, and thus we do not attempt to link it to the optical galaxy.

J1322+270: This is a nearby galaxy without detected radio lobes in the FIRST images. We find no reports of radio lobes in the literature either.

J1328+571: This low-mass ($M^* = 8 \times 10^8\, M_\odot$), low-redshift ($z_{\rm phot} = 0.032 \pm 0.029$) galaxy has many star-forming regions, at least two prominent arms, and a strong bar. With an estimated BH mass of $\lesssim 10^5\, M_\odot$, it qualifies as one of the very few intermediate-mass BHs known to have strong radio emission, and the first of its kind to have a double-lobed, extended jet structure. Greene et al. (2020) suggest that intermediate-mass BHs may not have sufficient time to sink into the galactic center by dynamical friction. This may explain why the center of the radio lobes is offset from the galactic nucleus by $\sim 4\farcs0$ (∼2.5 kpc).

J1349+454: We assign this galaxy to the low-confidence sample because only one lobe is detected. It does not satisfy our sample definition of double-lobed radio sources. Further observation may help to verify the existence of the other lobe.

J1354+465: This is a late-type galaxy with a stellar mass of $5 \times 10^9\, M_\odot$. Although classified into the low-confidence sample, it is still a strong candidate for radio association due to its proximity to the center of two radio lobes. Further high-resolution radio observations and optical spectroscopy to secure a better redshift would help to determine the optical–radio association.

J1509+515: This galaxy has two grand-design spiral arms, a long bar that reaches ∼10 kpc, and an enormous stellar mass of $5 \times 10^{11}\, M_\odot$. We consider it a low-confidence object because it is offset from the center of the radio lobes. However, we regard this galaxy as still a strong candidate, given its unusually large stellar mass.

J1633+084: This massive ($M_* = 2 \times 10^{11}\, M_\odot$), edge-on galaxy has a prominent, large-scale dust lane. It is quite unexpected that a galaxy this massive would have such a small bulge ($B/T = 0.11$), which is likely a pseudobulge given its very small Sérsic index ($n_{\rm bulge} = 0.37$). In addition to the two lobes, a prominent radio core is coincident with the optical galaxy. As both radio lobes are barely resolved, one might suspect that they are two unrelated point sources instead of radio lobes. However, the chance is extremely small for three unrelated sources to be so well aligned. We estimate the probability that three random radio sources with a projected distance smaller than $50''$ to be aligned by chance into a straight line with an accuracy of $5''$. As the FIRST survey has ∼220,000 resolved sources spanning 10,000 ${\rm deg^2}$ of the sky with ${\rm S/N} > 10$ (Banfield et al. 2015), the total number of such alignments is given by Edmunds & George (1981):

$$N = \frac{2\pi}{3} \Omega\, d^3\, n^3\, P, \tag{B1}$$

where Ω is the sky coverage of the survey, d is the maximum distance between the three sources, n is the source surface density, and P is the alignment accuracy. For this object, we find $N = 0.8$. Moreover, the actual probability is likely much lower as we find no optical counterparts for the two radio lobes. Therefore, it is unlikely that the three sources have no physical association, and we consider the two compact, symmetrically aligned radio sources to be radio lobes.

J1636+243: This faint galaxy (m_g = 20.1 mag) has a stellar mass of $3 \times 10^9\, M_\odot$. We classify it as a low-confidence source mainly because the number density of galaxies of that magnitude is large.

J1646+383: The galaxy has a prominent dust lane with a peculiar, arc-like shape. Curiously, we find a star projected against a radio contour, located northeast of the galaxy at (α, δ) = ($16^{\rm h}46^{\rm m}29\fs7$, $+38°31'36\farcs10$). The parallax measurement from Gaia of 0.44 ± 0.05 mas rules out the possibility that it is a quasar, and its SDSS colors ($u - g = 1.7$, $g - r = 0.6$) are consistent with those of a K-type star (Covey 2007). Thus, it is unlikely to be associated with the large-scale, intense radio emissions. Moreover, its Gaia proper motion of $v_{\rm N,E}$ = $(-3.3 \pm 0.1,\ 2.1 \pm 0.1)\ {\rm mas\ yr^{-1}}$ suggests that it is moving from northeast to southwest toward, instead of away from, the center of the radio lobes.

J1656+640: This extremely massive ($M_* = 3 \times 10^{11}\, M_\odot$) spiral galaxy, classified as star-forming from its narrow emission lines (Baldwin et al. 1981), has a star formation rate of $10\,M_{\odot}\,\mathrm{yr}^{-1}$ according to the GSWLA-2 catalog. A radio core coincides with the galactic nucleus, with an intensity slightly above 3σ. We note three other galaxies near the radio center, which are relatively low-redshift objects with $z_{\mathrm{phot}} < 0.3$, not likely distant giant elliptical galaxies.

J1721+262: The galaxy has a luminous bulge and an extended disk with spiral arms. A star, identified by the SDSS and Gaia, is projected to the south. The two radio hotspots have similar projected distances to the galaxy, with an extended tail emanating from the eastern one. A radio core coincides with the galaxy.

J2141+082: The galaxy has an interesting "eye-like" shape with a large stellar mass in excess of $10^{11}\,M_{\odot}$.

Appendix C
Two-dimensional Bulge–Disk Decomposition Images

We present the GALFIT bulge-to-disk decomposition results for 16 of the 18 sources in the high-confidence sample in Figure C1. Two galaxies are omitted: J0802+115 is a highly disturbed interacting system, for which no meaningful decomposition can be done, and J1328+571, which is a dwarf Magellanic spiral that has no detectable bulge.

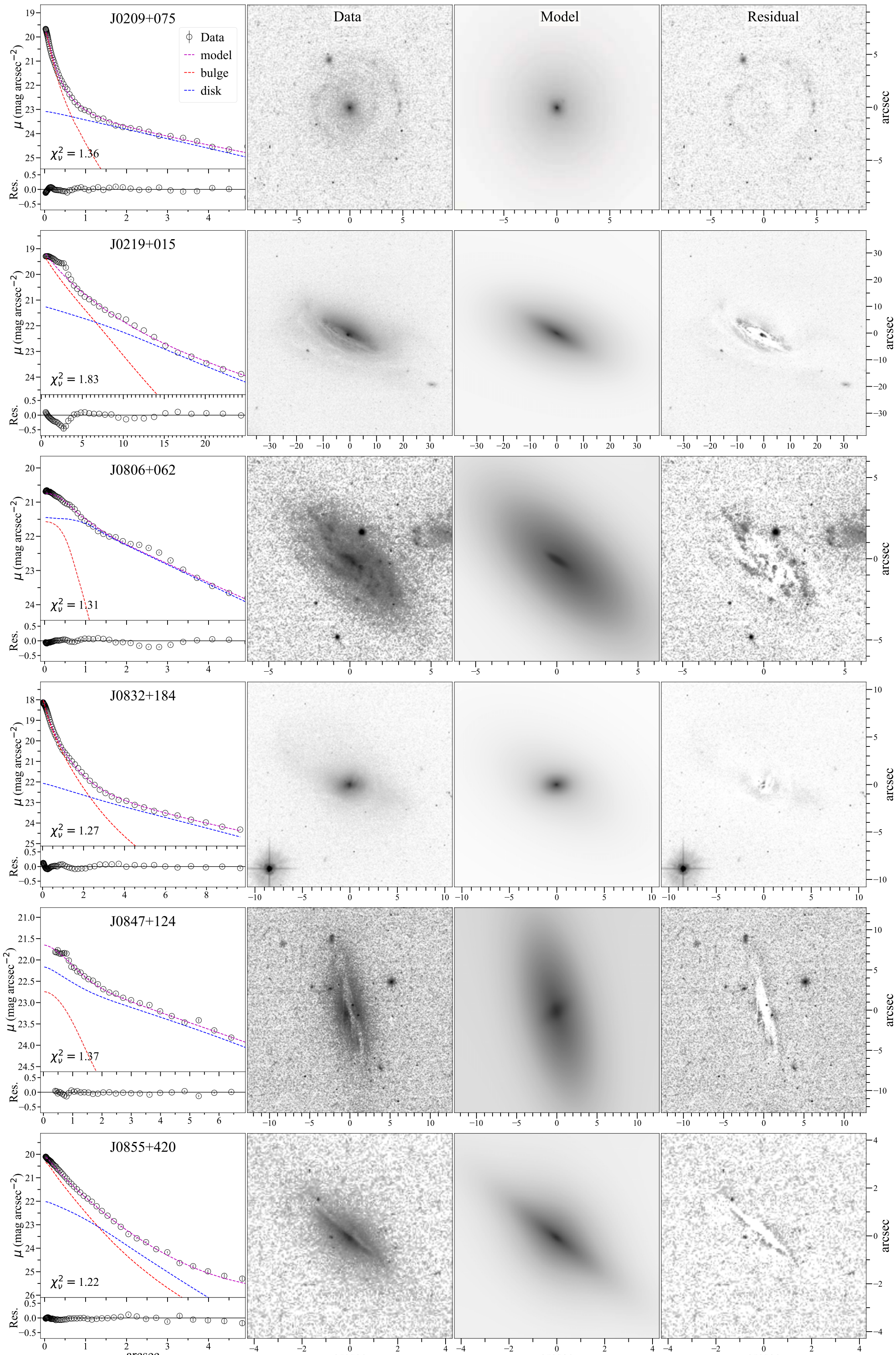

Figure C1. Two-dimensional bulge–disk decomposition using GALFIT of 16 of the 18 high-confidence sources in our sample. The left column shows the surface brightness profile of the data (open circles with error bars), Sérsic bulge component (red), exponential disk component (blue), and total (bulge + disk) model (purple). The χ^2_ν from GALFIT is shown in the lower-left corner. The lower panel gives the residuals between the data and the model. The right three columns show the original data, best-fit total model, and residuals, respectively. All images are displayed on a log stretch.

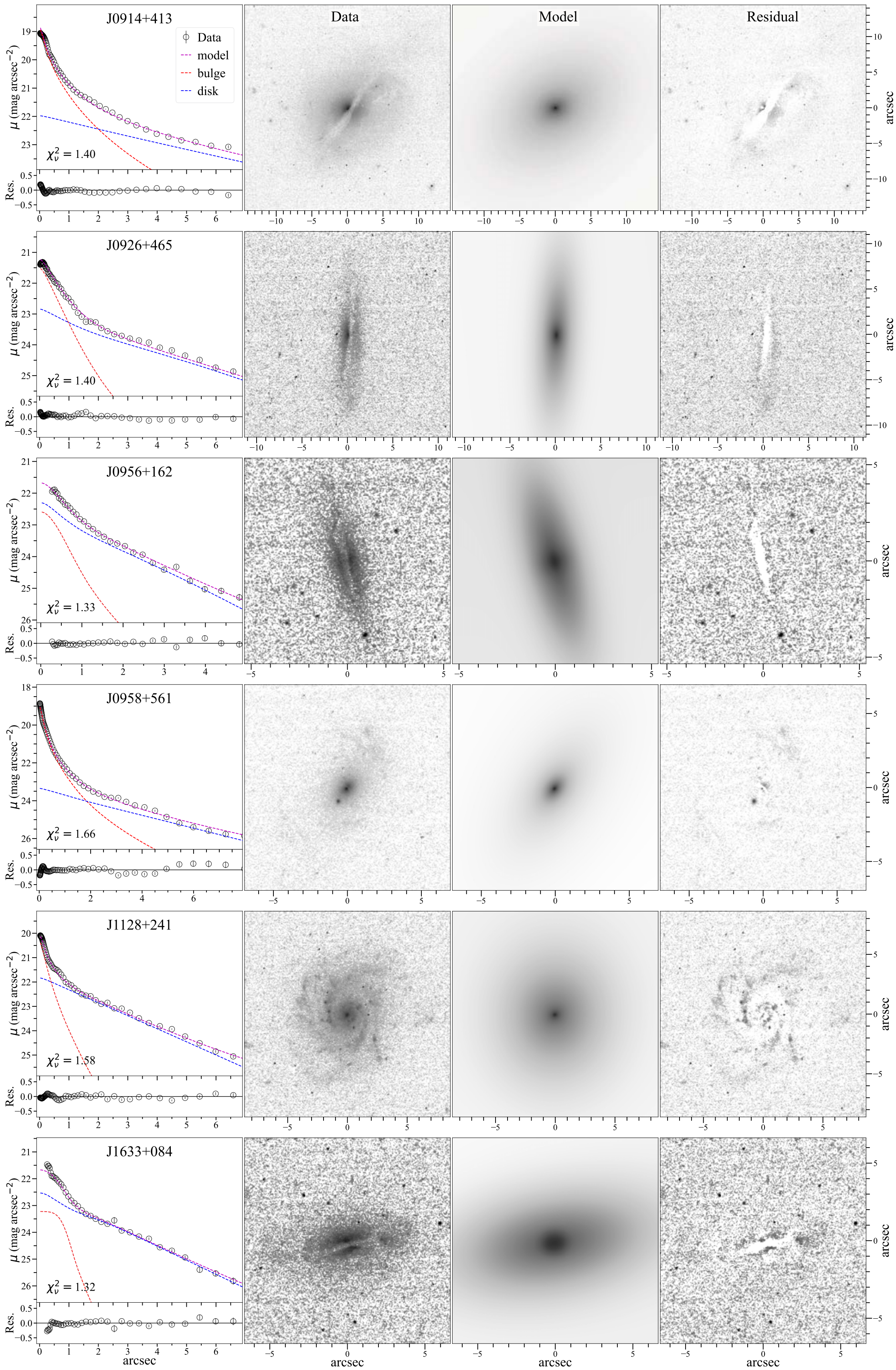

Figure C1. (Continued.)

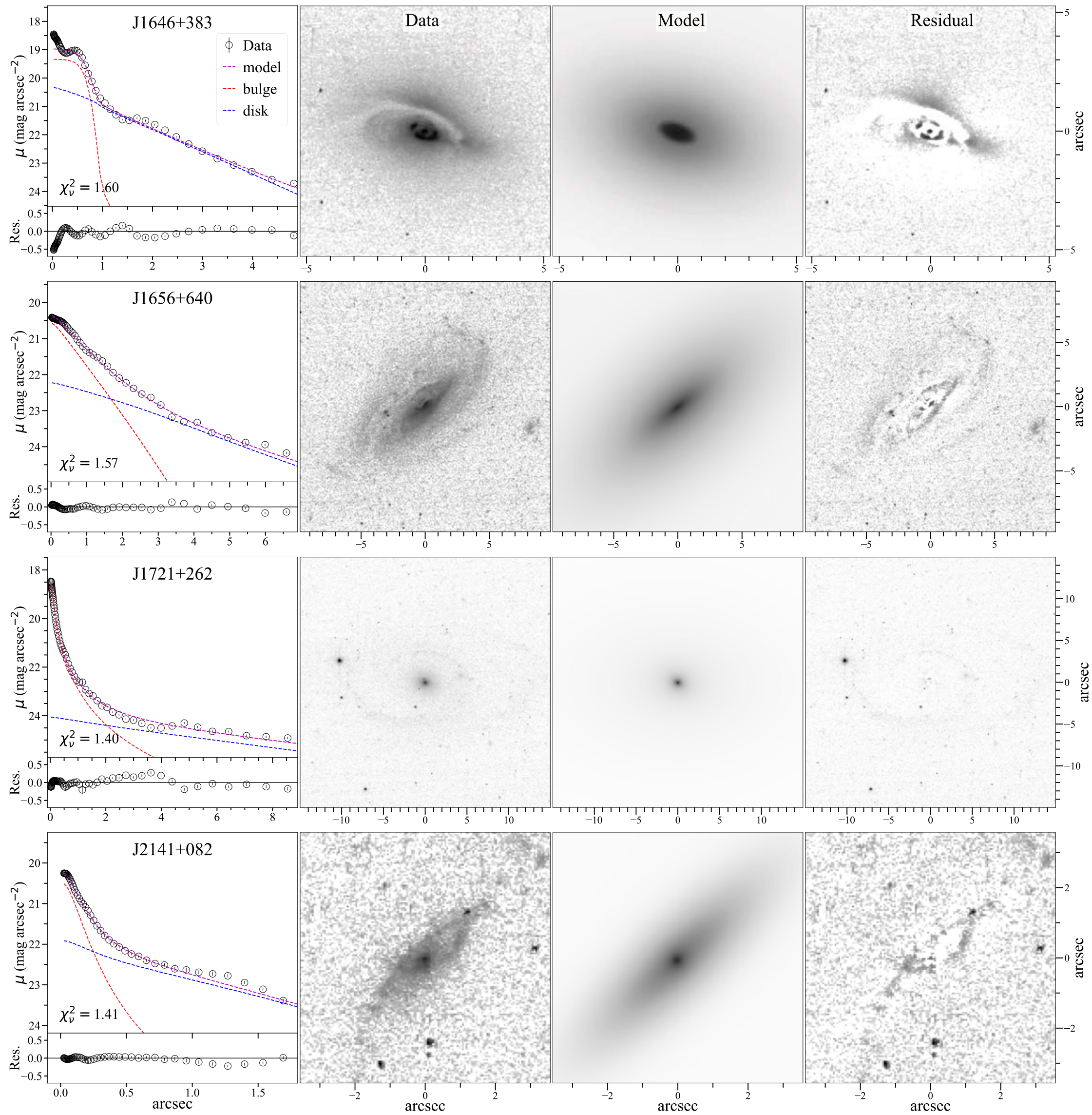

Figure C1. (Continued.)

ORCID iDs

Zihao Wu https://orcid.org/0000-0002-8876-5248
Luis C. Ho https://orcid.org/0000-0001-6947-5846
Ming-Yang Zhuang https://orcid.org/0000-0001-5105-2837

References

Abdo, A. A., Ackermann, M., Ajello, M., et al. 2009, ApJL, 707, L142
Ahn, C. P., Alexandroff, R., Allende Prieto, C., et al. 2014, ApJS, 211, 17
Akiyama, K., Alberdi, A., Alef, W., et al. 2022, ApJL, 930, L12
Alam, S., Albareti, F. D., Allende Prieto, C., et al. 2015, ApJS, 219, 12
Astropy Collaboration, Price-Whelan, A. M., Sipőcz, B. M., et al. 2018, AJ, 156, 123
Astropy Collaboration, Robitaille, T. P., Tollerud, E. J., et al. 2013, A&A, 558, A33
Baade, W., & Minkowski, R. 1954, ApJ, 119, 206
Bagchi, J., Vivek, M., Vikram, V., et al. 2014, ApJ, 788, 174
Baldwin, J. A., Phillips, M. M., & Terlevich, R. 1981, PASP, 93, 5
Banfield, J. K., Wong, O. I., Willett, K. W., et al. 2015, MNRAS, 453, 2326
Baum, S. A., Zirbel, E. L., & O'Dea, C. P. 1995, ApJ, 451, 88
Becker, R. H., White, R. L., & Helfand, D. J. 1995, ApJ, 450, 559
Bell, E. F., McIntosh, D. H., Katz, N., et al. 2003, ApJS, 149, 289
Bellstedt, S., Robotham, A. S. G., Driver, S. P., et al. 2020, MNRAS, 498, 5581
Berger, E. 2010, ApJ, 722, 1946
Best, P. N., & Heckman, T. M. 2012, MNRAS, 421, 1569
Best, P. N., Kauffmann, G., Heckman, T. M., et al. 2005, MNRAS, 362, 25
Birkinshaw, M., & Davies, R. L. 1985, ApJ, 291, 32
Blandford, R. D., & Znajek, R. L. 1977, MNRAS, 179, 433
Blanton, M. R., & Moustakas, J. 2009, ARAA, 47, 159
Bloom, J. S., Kulkarni, S. R., & Djorgovski, S. G. 2002, AJ, 123, 1111
Blundell, K. M., Rawlings, S., & Willott, C. J. 1999, AJ, 117, 677
Boquien, M., Burgarella, D., Roehlly, Y., et al. 2019, A&A, 622, A103
Boroson, T. A. 2002, ApJ, 565, 78
Bradley, L., Sipőcz, B., Robitaille, T., et al. 2020, astropy/photutils: 1.0.0, v1.0.0, Zenodo, doi:10.5281/zenodo.4044744
Brinchmann, J., Charlot, S., White, S. D. M., et al. 2004, MNRAS, 351, 1151
Browne, I. W. A., & Battye, R. A. 2010, in ASP Conf. Ser. 427, Accretion and Ejection in AGN: a Global View, 427, ed. L. Maraschi et al. (San Francisco, CA: ASP), 365
Buisson, D. J. K., Parker, M. L., Kara, E., et al. 2018, MNRAS, 480, 3689
Capetti, A., Massaro, F., & Baldi, R. D. 2017a, A&A, 598, A49
Capetti, A., Massaro, F., & Baldi, R. D. 2017b, A&A, 601, A81
Cardelli, J. A., Clayton, G. C., & Mathis, J. S. 1989, ApJ, 345, 245
Cavagnolo, K. W., McNamara, B. R., Nulsen, P. E. J., et al. 2010, ApJ, 720, 1066

Ceraj, L., Smolčić, V., Delvecchio, I., et al. 2018, A&A, 620, A192
Chabrier, G. 2003, ApJL, 586, L133
Chang, R., Gallazzi, A., Kauffmann, G., et al. 2006, MNRAS, 366, 717
Chilingarian, I. V., Melchior, A.-L., & Zolotukhin, I. Y. 2010, MNRAS, 405, 1409
Chilingarian, I. V., & Zolotukhin, I. Y. 2012, MNRAS, 419, 1727
Chilingarian, I. V., Zolotukhin, I. Y., Katkov, I. Y., et al. 2017, ApJS, 228, 14
Conselice, C. J. 2003, ApJS, 147, 1
Conselice, C. J. 2014, ARA&A, 52, 291
Covey, K. R., Ivezić, Ž., Schlegel, D., et al. 2007, AJ, 134, 2398
Crookston, N. L., & Finley, A. O. 2008, J. Stat. Softw., 23, 1
de Vaucouleurs, G. 1948, AnAp, 11, 247
Dey, A., Schlegel, D. J., Lang, D., et al. 2019, AJ, 157, 168
Duncan, K. J. 2022, MNRAS, 512, 3662
Dunlop, J. S., McLure, R. J., Kukula, M. J., et al. 2003, MNRAS, 340, 1095
Edmunds, M. G., & George, G. H. 1981, Natur, 290, 481
Fanaroff, B. L., & Riley, J. M. 1974, MNRAS, 167, 31P
Filippenko, A. V., & Ho, L. C. 2003, ApJL, 588, L13
Fisher, D. B., & Drory, N. 2008, AJ, 136, 773
Fisher, D. B., & Drory, N. 2016, ASSL, 418, 41
Ford, H. C., Bartko, F., Bely, P. Y., et al. 1998, Proc. SPIE, 3356, 234
Foschini, L., Berton, M., Caccianiga, A., et al. 2015, A&A, 575, A13
Franceschini, A., Vercellone, S., & Fabian, A. 1998, MNRAS, 297, 817
Fukugita, M., Shimasaku, K., & Ichikawa, T. 1995, PASP, 107, 945
Gadotti, D. A. 2009, MNRAS, 393, 153
Gaia Collaboration, Brown, A. G. A., Vallenari, A., et al. 2021, A&A, 649, A1
Gao, H., & Ho, L. C. 2017, ApJ, 845, 114
Gao, H., Ho, L. C., Barth, A. J., et al. 2018, ApJ, 862, 100
Gao, H., Ho, L. C., Barth, A. J., et al. 2019, ApJS, 244, 34
Gao, H., Ho, L. C., Barth, A. J., et al. 2020, ApJS, 247, 20
Gao, H., Ho, L. C., & Li, Z.-Y. 2022, ApJS, 262, 54
Gavazzi, G., & Boselli, A. 1999, A&A, 343, 86
Ghisellini, G., & Celotti, A. 2001, A&A, 379, L1
Graham, J. A. 1979, ApJ, 232, 60
Greene, J. E., & Ho, L. C. 2004, ApJ, 610, 722
Greene, J. E., Ho, L. C., & Ulvestad, J. S. 2006, ApJ, 636, 56
Greene, J. E., Strader, J., & Ho, L. C. 2020, ARA&A, 58, 257
Hamilton, T. S., Casertano, S., & Turnshek, D. A. 2002, ApJ, 576, 61
Harris, C. R., Millman, K. J., van der Walt, S. J., et al. 2020, Natur, 585, 357
Häußler, B., Bamford, S. P., Vika, M., et al. 2013, MNRAS, 430, 330
Häußler, B., Vika, M., Bamford, S. P., et al. 2022, AA, 664, A92
Heckman, T. M. 1980, A&A, 87, 152
Hinshaw, G., Larson, D., Komatsu, E., et al. 2013, ApJS, 208, 19
Ho, L. C. 2002, ApJ, 564, 120
Ho, L. C. 2008, ARA&A, 46, 475
Ho, L. C., Li, Z.-Y., Barth, A. J., Seigar, M. S., & Peng, C. Y. 2011, ApJS, 197, 21
Ho, L. C., & Peng, C. Y. 2001, ApJ, 555, 650
Ho, L. C., & Ulvestad, J. S. 2001, ApJS, 133, 77
Holwerda, B. W., Kelvin, L., Baldry, I., et al. 2019, AJ, 158, 103
Hooper, E. J., Impey, C. D., Foltz, C. B., & Hewett, P. C. 1995, ApJ, 445, 62
Hota, A., Sirothia, S. K., Ohyama, Y., et al. 2011, MNRAS, 417, L36
Huchra, J. P., Vogeley, M. S., & Geller, M. J. 1999, ApJS, 121, 287
Jackson, R. A., Kaviraj, S., Martin, G., et al. 2022, MNRAS, 511, 607
Jackson, R. A., Martin, G., Kaviraj, S., et al. 2020, MNRAS, 494, 5568
Järvelä, E., Lähteenmäki, A., & Berton, M. 2018, A&A, 619, A69
Jester, S., Schneider, D. P., Richards, G. T., et al. 2005, AJ, 130, 873
Jiang, J., Walton, D. J., Fabian, A. C., & Parker, M. L. 2019, MNRAS, 483, 2958
Kauffmann, G., Heckman, T. M., Tremonti, C., et al. 2003, MNRAS, 346, 1055
Kawinwanichakij, L., Silverman, J. D., Ding, X., et al. 2021, ApJ, 921, 38
Keel, W. C., Tate, J., Wong, O. I., et al. 2022, AJ, 163, 150
Keel, W. C., White, R. E., III, Owen, F. N., & Ledlow, M. J. 2006, AJ, 132, 2233
Kellermann, K. I., Sramek, R. A., Schmidt, M., Shaffer, D. B., & Green, R. F. 1989, AJ, 98, 1195
Kelvin, L. S., Driver, S. P., Robotham, A. S. G., et al. 2014, MNRAS, 444, 1647
Kewley, L. J., Dopita, M. A., Sutherland, R. S., et al. 2001, ApJ, 556, 121
Kewley, L. J., Groves, B., Kauffmann, G., & Heckman, T. 2006, MNRAS, 372, 961
Kim, M., Ho, L. C., Peng, C. Y., Barth, A. J., & Im, M. 2017, ApJS, 232, 21
Kinney, A. L., Calzetti, D., Bohlin, R. C., et al. 1996, ApJ, 467, 38
Kormendy, J. 1977, ApJ, 218, 333
Kormendy, J. 2016, in Galactic Bulges, ed. E. Laurikainen, R. Peletier, & D. Gadotti (New York: Springer), 431
Kormendy, J., & Ho, L. C. 2013, ARA&A, 51, 511
Kormendy, J., & Kennicutt, R. C. 2004, ARA&A, 42, 603
Kotilainen, J. K., Tavares, J. L., Olguin-Iglesias, A., et al. 2016, ApJ, 832, 157
Lacy, M., Laurent-Muehleisen, S. A., Ridgway, S. E., Becker, R. H., & White, R. L. 2001, ApJL, 551, L17
Laing, R. A., Riley, J. M., & Longair, M. S. 1983, MNRAS, 204, 151
Ledlow, M. J., & Owen, F. N. 1996, AJ, 112, 9
Ledlow, M. J., Owen, F. N., & Eilek, J. A. 2002, NewAR, 46, 343
Ledlow, M. J., Owen, F. N., & Keel, W. C. 1998, ApJ, 495, 227
León-Tavares, J., Kotilainen, J., Chavushyan, V. H., et al. 2014, ApJ, 795, 58
Li, Z.-Y., Ho, L. C., Barth, A. J., et al. 2011, ApJS, 197, 22
Loveday, J., Norberg, P., Baldry, I. K., et al. 2012, MNRAS, 420, 1239
Loveday, J., Norberg, P., Baldry, I. K., et al. 2015, MNRAS, 451, 1540
Luo, Q., & Sadler, E. M. 2010, ApJ, 713, 398
Magorrian, J., Tremaine, S., Richstone, D., et al. 1998, AJ, 115, 2285
Mao, M. Y., Owen, F., Duffin, R., et al. 2015, MNRAS, 446, 4176
Marinucci, A., Matt, G., Miniutti, G., et al. 2014, ApJ, 787, 83
Matthews, T. A., Morgan, W. W., & Schmidt, M. 1964, ApJ, 140, 35
Mauch, T., & Sadler, E. M. 2007, MNRAS, 375, 931
McCaffrey, T. V., Kimball, A. E., Momjian, E., et al. 2022, AJ, 164, 122
McLure, R. J., & Jarvis, M. J. 2004, MNRAS, 353, L45
McLure, R. J., Kukula, M. J., Dunlop, J. S., et al. 1999, MNRAS, 308, 377
McLure, R. J., Willott, C. J., Jarvis, M. J., et al. 2004, MNRAS, 351, 347
McMahon, R. G., White, R. L., Helfand, D. J., & Becker, R. H. 2002, ApJS, 143, 1
McMullin, J. P., Waters, B., Schiebel, D., et al. 2007, in ASP Conf. Ser. 376, Astronomical Data Analysis Software and Systems XVI, ed. R. A. Shaw, F. Hill, & D. J. Bell (San Francisco, CA: ASP), 127
Miller, L., Peacock, J. A., & Mead, A. R. G. 1990, MNRAS, 244, 207
Mirabel, I. F., & Rodríguez, L. F. 1999, ARA&A, 37, 409
Mirakhor, M. S., Walker, S. A., Bagchi, J., et al. 2021, MNRAS, 500, 2503
Moffett, A. J., Ingarfield, S. A., Driver, S. P., et al. 2016, MNRAS, 457, 1308
Mulcahy, D. D., Mao, M. Y., Mitsuishi, I., et al. 2016, A&A, 595, L8
Narayan, R., & Yi, I. 1994, ApJL, 428, L13
Neumann, J., Wisotzki, L., Choudhury, O. S., et al. 2017, AA, 604, A30
Ocran, E. F., Taylor, A. R., Vaccari, M., et al. 2021, MNRAS, 500, 4685
Ogle, P. M., Lanz, L., Appleton, P. N., Helou, G., & Mazzarella, J. 2019, ApJS, 243, 14
Ogle, P. M., Lanz, L., Nader, C., & Helou, G. 2016, ApJ, 817, 109
Olguín-Iglesias, A., Kotilainen, J. K., & Chavushyan, V. 2020, MNRAS, 492, 1450
Orban de Xivry, G., Davies, R., Schartmann, M., et al. 2011, MNRAS, 417, 2721
Owen, F. N., & Ledlow, M. J. 1994, in ASP Conf. Ser. 54, The First Stromlo Symp.: The Physics of Active Galaxies, ed. G. V. Bicknell, M. A. Dopita, & P. J. Quinn (San Francisco, CA: ASP), 319
Padovani, P. 2017, NatAs, 1, 194
Peng, C. Y., Ho, L. C., Impey, C. D., & Rix, H.-W. 2002, AJ, 124, 266
Peng, C. Y., Ho, L. C., Impey, C. D., & Rix, H.-W. 2010, AJ, 139, 2097
Petrosian, V. 1976, ApJL, 210, L53
Prescott, M., Mauch, T., Jarvis, M. J., et al. 2016, MNRAS, 457, 730
Reynolds, C. S. 2019, NatAs, 3, 41
Reynolds, C. S. 2021, ARA&A, 59, 117
Rizzo, M. L. 2019, Statistical computing with R (New York: Chapman and Hall/CRC)
Rodriguez-Gomez, V., Snyder, G. F., Lotz, J. M., et al. 2019, MNRAS, 483, 4140
Sachdeva, S., Ho, L. C., Li, Y., & Shankar, F. 2020, ApJ, 899, 89
Sadler, E. M., Jackson, C. A., Cannon, R. D., et al. 2002, MNRAS, 329, 227
Salim, S., Boquien, M., & Lee, J. C. 2018, ApJ, 859, 11
Salim, S., Lee, J. C., Janowiecki, S., et al. 2016, ApJS, 227, 2
Sandage, A. R., Freeman, K. C., & Stokes, N. R. 1970, ApJ, 160, 831
Scarpa, R., & Urry, C. M. 2001, ApJ, 556, 749
Schechter, P. L. 1976, ApJ, 203, 297
Schlafly, E. F., & Finkbeiner, D. P. 2011, ApJ, 737, 103
Sérsic, J. L. 1968, Atlas de Galaxias Australes (Córdoba: Obs. Astron., Univ. Nac. Córdoba)
Shakura, N. I., & Sunyaev, R. A. 1973, A&A, 24, 337
Singh, V., Ishwara-Chandra, C. H., Sievers, J., et al. 2015, MNRAS, 454, 1556
STScI Development Team 2013, pysynphot: Synthetic photometry software package, Astrophysics Source Code Library, ascl:1303.023
Tadhunter, C. 2016, A&ARv, 24, 10
Taylor, E. N., Hopkins, A. M., Baldry, I. K., et al. 2011, MNRAS, 418, 1587
Toomre, A., & Toomre, J. 1972, ApJ, 178, 623

Ulvestad, J. S., Antonucci, R. R. J., & Goodrich, R. W. 1995, AJ, 109, 81
Ulvestad, J. S., & Ho, L. C. 2001, ApJ, 558, 561
Urry, C. M., & Padovani, P. 1995, PASP, 107, 803
Urry, C. M., Scarpa, R., O'Dowd, M., et al. 2000, ApJ, 532, 816
van der Marel, R. P., Alves, D. R., Hardy, E., & Suntzeff, N. B. 2002, AJ, 124, 2639
Vasudevan, R. V., Fabian, A. C., Reynolds, C. S., et al. 2016, MNRAS, 458, 2012
Vietri, A., Järvelä, E., Berton, M., et al. 2022, AA, 662, A20
Visnovsky, K. L., Impey, C. D., Foltz, C. B., et al. 1992, ApJ, 391, 560
Walton, D. J., Risaliti, G., Harrison, F. A., et al. 2014, ApJ, 788, 76
Whittam, I. H., Jarvis, M. J., Hale, C. L., et al. 2022, MNRAS, 516, 245
Wilson, A. S., & Colbert, E. J. M. 1995, ApJ, 438, 62
Woo, J.-H., & Urry, C. M. 2002, ApJ, 579, 530
Wright, E. L., Eisenhardt, P. R. M., Mainzer, A. K., et al. 2010, AJ, 140, 1868
Wrobel, J. M., & Ho, L. C. 2006, ApJL, 646, L95
Yang, X., Joshi, R., Gopal-Krishna, et al. 2019, ApJS, 245, 17
Zeng, G., Wang, L., & Gao, L. 2021, MNRAS, 507, 3301
Zhuang, M.-Y., & Ho, L. C. 2022, ApJ, 934, 145
Zirbel, E. L. 1996, ApJ, 473, 713